TYPE II BAND ALIGNMENT IN $SI_{1-X}GE_X/SI(001)$ QUANTUM WELLS

by

Christoph F. Reinhart
B.Sc. Trent University, 1995

Thesis Submitted in Partial Fulfillment of
The Requirements for the Degree of
MASTER OF SCIENCE
in the Department of Physics

© Christoph F. Reinhart
SIMON FRASER UNIVERSITY
April 1997

All rights reserved. This work may not be
reproduced in whole or in part, by photocopy
or other means, without permission of the author.

National Library of Canada

Acquisitions and Bibliographic Services

395 Wellington Street
Ottawa ON K1A 0N4
Canada

Bibliothèque nationale du Canada

Acquisitions et services bibliographiques

395, rue Wellington
Ottawa ON K1A 0N4
Canada

Your file Votre référence

Our file Notre référence

The author has granted a non-exclusive licence allowing the National Library of Canada to reproduce, loan, distribute or sell copies of this thesis in microform, paper or electronic formats.

L'auteur a accordé une licence non exclusive permettant à la Bibliothèque nationale du Canada de reproduire, prêter, distribuer ou vendre des copies de cette thèse sous la forme de microfiche/film, de reproduction sur papier ou sur format électronique.

The author retains ownership of the copyright in this thesis. Neither the thesis nor substantial extracts from it may be printed or otherwise reproduced without the author's permission.

L'auteur conserve la propriété du droit d'auteur qui protège cette thèse. Ni la thèse ni des extraits substantiels de celle-ci ne doivent être imprimés ou autrement reproduits sans son autorisation.

0-612-24230-7

Canada

ABSTRACT:

The question of the nature of the conduction band (CB) edge alignment of strained SiGe heterostructures on (001)Si has remained unanswered, in spite of numerous attempts to resolve it. This thesis presents experimental evidence confirming type II CB alignment in a commensurate 30 Å $Si_{0.7}Ge_{0.3}$ Si (001) single quantum well (QW) grown by ultra-high vacuum-chemical vapor deposition.

Low-temperature near-gap photoluminescence (PL) spectra of externally strained samples are recorded over a wide range of excitation power densities. To interpret the experimental findings, detailed deformation potential calculations are carried out and reveal that the application of biaxial (001) and uniaxial [110] strain causes opposite energy shifts in the SiGe PL for type I and type II CB offsets. The measured PL signal from the single QW exhibits a dramatic change from type II to type I behavior for increasing excitation densities. We attribute this changeover to band bending, caused by charge accumulation of the confined holes in the SiGe QW. The observed redshift of the SiGe PL under low excitation conditions can only be explained by a type II band alignment.

Additional characteristics are a remarkable and yet unexplained enhancement in the SiGe transverse acoustic (TA) phonon replica, and a reduction in the intensity of the Ge-Ge and Si-Ge transverse optical (TO) phonon replicas relative to the Si-Si mode.

DEDICATION

To Diana,

my sunny day in Vancouver

my inspiration

my real life

To my Parents

my inexhaustible source of security and care[1]

---

[1] *and cash*

ACKNOWLEDGMENT

I want to thank my senior supervisor Dr. Mike Thewalt for sharing his physical insight and numerous lab skills with me. His deep experimental interest and omnipresence in the lab create an effective research environment in a generous labs setting. I feel very fortunate to have been given the opportunity to work on a great project that lead to a new physical concept and promising device applications.

Special thanks to Dale Harrison who has worked all along together with me on this project and who introduced me to many useful experimental skills. Without him, my work in the lab would not have been the same.

I enjoyed a very relaxed working environment due to my other fellow students in the lab. Cheers boys! Thanks to Sharon Beever for being a constant help with all the paper work that comes with a degree completion. Hey Ted, my afternoons would have been incomplete without our coffee breaks. Thanks to Dale and Ted for proof reading my thesis and eliminating the numerous language bugs.

Moneywise, several Research Assistantships from Mike Thewalt and a Graduate Fellowship from Simon Fraser University have been greatly appreciated and happily spent.

TABLE OF CONTENTS

APPROVAL......II
ABSTRACT......III
DEDICATION......IV
ACKNOWLEDGMENT......V
LIST OF FIGURES......VIII
LIST OF TABLES......IX

I. INTRODUCTION 1

II. SILICON, GERMANIUM AND THEIR ALLOYS 3

II.A. SILICON 3
II.B. GERMANIUM 4
II.C. SILICON GERMANIUM 5
II.D. STRAINED Si/SiGe HETEROSTRUCTURES 6
II.D.1. QUANTUM WELLS 7
II.E. MOTIVATION FOR THIS STUDY 8
II.F. PAST EXPERIMENTAL AND THEORETICAL ATTEMPTS TO DETERMINE Δ_c 9
II.G. SUMMARY 12

III. EXCITONS AND PHOTOLUMINESCENCE IN A Si/SiGe QUANTUM WELL 13

III.A. EXCITONS AND PHOTOLUMINESCENCE 13
III.B. PHOTOLUMINESCENCE IN RELAXED SiGe 15
III.C. PHOTOLUMINESCENCE IN STRAINED SiGe 16
III.D. SUMMARY 18

IV. EXPERIMENTAL TECHNIQUES 19

IV.A. SAMPLES 19
IV.B. EXCITATION SOURCE 21
IV.C. DEWAR 22
IV.D. STRAIN GEOMETRIES 23
IV.D.1. UNIAXIAL STRESS ALONG [110] 23
IV.D.2. BIAXIAL STRESS ALONG (001) 24
IV.E. SPECTRAL ANALYZER AND DETECTOR 25
IV.E.1. FOURIER TRANSFORM SPECTROSCOPY 25
IV.E.2. DISPERSIVE SPECTROSCOPY 28
IV.E.3. COMPARISON BETWEEN DISPERSIVE AND FOURIER TRANSFORM SPECTROSCOPY 29
IV.F. TIME-RESOLVED PHOTOLUMINESCENCE 29

IV.G. PROCEDURE 30

V. PHOTOLUMINESCENCE SPECTRA UNDER STRAIN 31

V.A. FROM STRESS TO STRAIN 32
V.A.1. STRESS 32
V.A.2. STRAIN 33
V.A.3. STRAIN IN THE TWO BENDING GEOMETRIES 34
V.B. THE EFFECT OF STRAIN ON ENERGY BANDS 38
V.B.1. HYDROSTATIC DEFORMATION POTENTIAL 39
V.B.2. VALENCE BAND SPLITTING 39
V.B.3. CONDUCTION BAND SPLITTING 41
V.C. CALCULATION OF THE ENERGY SHIFTS 43
V.C.1. BIAXIAL STRAIN : 43
V.C.2. UNIAXIAL STRAIN : 48
V.D. SUMMARY: 50

VI. EXPERIMENTAL RESULTS AND DISCUSSION 52

VI.A. ENERGY SHIFTS OF THE SiGe PL UNDER EXTERNAL STRAIN 52
VI.B. TIME-RESOLVED PL 55
VI.C. TYPE I/TYPE II SPECTRA 57
VI.D. THE TA/TO$_{Si-Si}$ RATIO IN TYPE I/II SPECTRA 60
VI.E. DISCUSSION 62
VI.F. SUMMARY AND OUTLOOK 64

REFERENCES 65

LIST OF FIGURES

Figure I-1: Type I or Type II Band Alignment in strained $Si_{1-x}Ge_x$ on Si 1

Figure IV-1: Schematic of Uniaxial and Biaxial Bending Rigs 24

Figure IV-2: Configuration for the Fourier Transform Spectroscopy 25

Figure IV-3: Configuration for the Dispersive Spectroscopy 28

Figure V-1: Transitions due to a Type I and Type II Band Alignment 32

Figure V-2: Effect of Strain on the Si and SiGe Lattices...............................36

Figure V-3: Theoretical Behavior of the Bands under Biaxial Strain..........47

Figure V-4: Theoretical Behavior of the Bands under Uniaxial Strain 51

Figure VI-1: Experimental Energy Shifts of SiGe under External Strain 53

Figure VI-2: Qualitative Model of Band Bending 56

Figure VI-3: Decay of the SiGE PL Signal with Time.....................................58

Figure VI-4: PL Spectra versus Excitation Density from Strained SiGe/Si .61

Figure VI-5: Type I/II Spectra from various Samples....................................62

LIST OF TABLES:

Table V-1: Three Dimensional Lattice Types 36

Table V-2: Strain Components and Compliances induced by Uniaxial and Biaxial Strain for Si and $Si_{0.7}Ge_{0.3}$ 38

Table V-3: Deformation Potential Constants for Si and $Si_{0.7}Ge_{0.3}$ 46

Table V-4: Numerical Comparison between δE110 and δE 49

SYMBOLS

BE	bound excitons
BS	beam splitter
CB	conduction band
Δ_C	conduction band offset
Δ_V	valence band offset
fcc	face centered cubic
FWHM	full width half maximum
HBT	heterojunction bipolar transistor
LO/LA	longitudinal optical / acoustic
BMEC	bound multiple exciton complex
NP	no phonon
PL	photoluminescence
QW	quantum well
TO	transverse optical
VB	valence band
ZDP	zero path difference

I. Introduction

The main question discussed and answered in this thesis is whether the band alignment of a commensurate $Si/Si_{1-x}Ge_x$ interface is type I or type II. The band gap of $Si_{1-x}Ge_x$ lies between the band gap of silicon and germanium (1.17 eV and 0.89 eV at T= 0K). There is a general agreement that the size of the conduction band offset (Δ_C) is much smaller than the size of the valence band offset (Δ_V) which is positive [84P], [89Wb], [91R],[93F]. The remaining debate is concerned with he sign of Δ_C, shown in Figure I-1 (type I: $\Delta_C<0$; type II: $\Delta_C>0$).

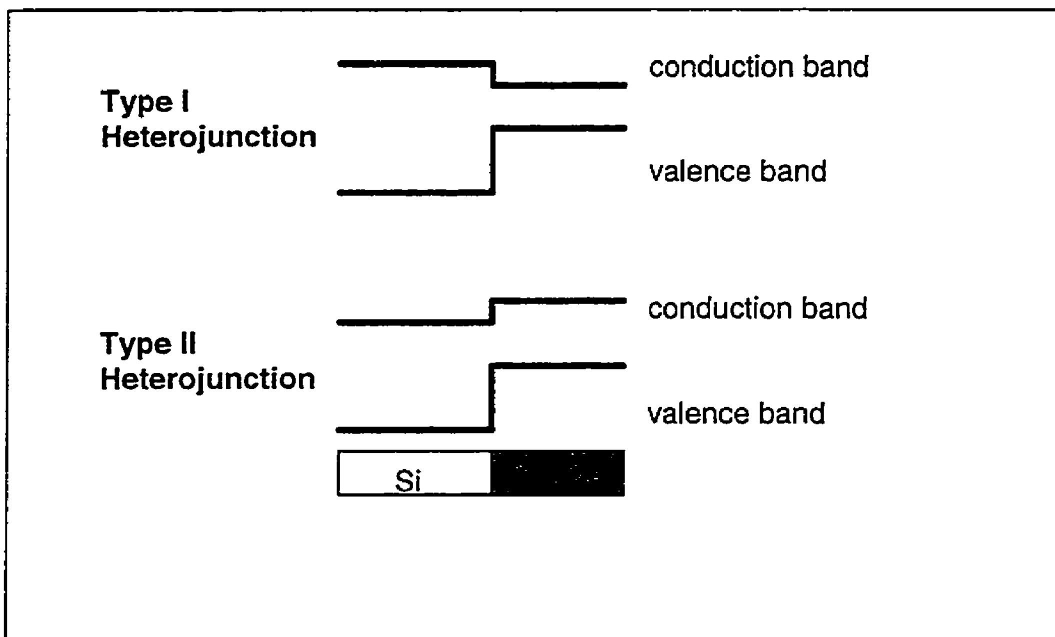

***Figure I-1:** Is the band alignment of a strained Si_{1-x} Ge_x on Si heterostructure type I or type II?*

This work describes an experimental test that has found type II band alignment for a pseudomorphically grown Si/$Si_{0.7}Ge_{0.3}$/Si quantum well, in contrast to recent claims of a type I alignment [95H].

Thesis outline:

Section II serves as an introduction to Si, Ge and strained $Si_{1-x}Ge_x$ on Si. It also describes some devices based on these materials. Section III reviews the physics of low temperature photoluminescence spectroscopy, followed by section IV in which the utilized experimental setup and procedures are described. Section V gives a detailed account of the theoretical energy shifts of the photoluminescence signal of a SiGe quantum well under external strain for the cases of a type I or type II band alignment. Finally, section VI presents experimental results that confirm a type II band alignment in the investigated quantum well structure.

II. Silicon, Germanium and their Alloys

This chapter introduces the reader to the basic electrical and optical properties of silicon, germanium and their alloys. Section II-D deals with the growth of SiGe on Si and is followed by a survey of silicon based heterostructures in order to further motivate this study. Section II-F summarizes past attempts to measure or calculate the sign of Δ_c.

II.A. Silicon

Silicon (Si) is the second most abundant element in the Earth's crust, where it is mainly found as an oxide in the form of quartz and sand. SiO_2 is commercially reduced with carbon and afterwards purified by zone melting and fractional distillation to as low as one impurity in $2x10^{11}$ silicon atoms [84G]. Single crystal ingots are produced by pulling the crystal out of the melt (Czochralski process) or by floating zone crystal growth. High-purity single crystal silicon can be selectively doped with boron, gallium, phosphorus, or arsenic by diffusion techniques or ion implantation. Its natural abundance, low cost and impressive manufacturing possibilities make silicon the dominant element in electronic devices like solar cells, conventional transistors, integrated circuits and rectifiers.

Silicon is an indirect band gap semiconductor, (i.e. its conduction band minimum and valence band maximum lie at different positions in k-space) and as a result, inter band-edge transitions have to be assisted by crystal momentum

conserving phonons. Such processes are inherently less efficient than those in a direct band gap semiconductor like GaAs. Hence, Si is outperformed by the family of III-V compound semiconductors in the domain of opto electronics (e.g. for optical emitters and detectors). Another drawback of silicon is its relatively low electron mobility (μ_{Si} =1500 cm^2/Vs^{-1}; μ_{GaAs} =8500 cm^2/Vs^{-1} [!] [69S]), which slows down the operating speed of a silicon-based device. Furthermore, epitaxial GaAs can be grown in alternation with other materials such as AlAs and $Ga_{1-x}Al_xAs$. These semiconductor heterostructures have more degrees of freedom than Si, since they allow band gap engineering. On the other hand, an obvious disadvantage of GaAs is its high cost of ~20$US/in^2 [#] (about 5 times higher than Si [96M]) and the environmentally dubious nature of As [81W]. Also, the high quality oxide layer on Si is very important both for the manufacturing of integrated circuits, as well as for making MOS transistors. In order to overcome the limitations in silicon-based devices, SiGe alloys seem to be a natural heterostructure match for Si [85B].

II.B. Germanium

Germanium (Ge) is below silicon in the periodic table, i.e. it is also four-valent. It can be recovered as a byproduct from the combustion of certain coals and is commercially purified, just like silicon, by fractional distillation of its

---

[!] mobilities of the intrinsic bulk semiconductors at 300 K
[#] approximate cost of a in^2 of GaAs substrate

tetrachloride to one impurity in 10^{10} atoms [81W]. Germanium has a band gap of 0.83 eV at 300 K, which makes it suitable for infrared detection.

II.C. Silicon Germanium

Si and Ge can freely be mixed, since they are chemically compatible and form bonding orbitals that are called sp^3 hybrids. Like Si and Ge, $Si_{1-x}Ge_x$ crystallizes in the diamond lattice. This structure has a fcc (face centered cubic) lattice with a two atom basis in which the atoms are located at (000) and $a_0/4(111)$; a_0 being the lattice constant of the material. In the alloy, the two elements distribute themselves randomly on the positions of the crystal lattice. A relaxed $Si_{1-x}Ge_x$ bulk sample has a crystal lattice constant that varies linearly between a_{Si}= 5.43Å and a_{Ge}= 5.65Å with the Germanium content of the alloy [86vdW]. For both elements and all their alloys, the VB maxima lie at the origin of k-space. The most important difference between the two band diagrams is that the six (eight) conduction band mimima of Si (Ge) lie along the <001> (<111>) directions, respectively. Although SiGe lacks perfect translational symmetry, many of its properties can be understood by applying band structure concepts and treating the composition irregularities as a perturbation. The first comprehensive study over the whole alloy composition range of unstrained bulk SiGe has been carried out by Weber and Alonso [89WB] who measured the indirect band gap of unstrained $Si_{1-x}Ge_x$ using photoluminescence (PL) . The

conduction band structure of SiGe[#] is silicon-like for germanium contents below about 86% [86vdW]. At that composition the CB minima change from the <001>-type valleys of the Si to the <111>-type valleys of the Ge conduction band minima [85P]. In the present study only $Si_{0.7}Ge_{0.3}$ layers are considered (i.e. the band gap is always silicon-like).

II.D. Strained Si/SiGe heterostructures

In the previous section, we saw that SiGe is a promising material to form heterostructures with Si. The major problem in growing $Si_{1-x}Ge_x$ on Si is the large lattice mismatch between Si and Ge (>4%). Two energies are competing in the growth process of SiGe on bulk Si:

- The SiGe can form a crystal with a lattice constant equal to Si parallel to the interface and store elastic energy that grows with the layer thickness. This lattice mismatch is accommodated by a homogeneous tetragonal strain in the alloy. The in-plane compression is compensated by a widening of the SiGe cubic planes to reduce some of the elastic energy stored in the crystal.
- The other possibility is that dislocations appear at the interface that allow the SiGe to relax to its bulk form. These *misfit dislocations* have a significant energy associated with them.

[#] In the following, the subscripts, x and 1-x, will be dropped for convenience, unless necessary.

Hence, the initial growth mode of the SiGe is pseudomorphic or *commensurate* until a critical thickness is reached, i.e. until the stored elastic energy outweighs the energy expense of dislocations. This critical thickness is about 80 Å for a Ge content of 30% [85P1]. However, dislocation free SiGe films are routinely grown whose thicknesses exceed the equilibrium critical thickness by more than an order of magnitude [92S1]. Attempts to predict this *metastable critical thickness* are so far of a phenomenological nature [96A].

For device purposes, dislocations have to be avoided, since they produce undesirable electrical activity, i.e. they act as traps for mobile electrons or holes. Therefore, SiGe layers, integrated in heterostructure devices, have to be kept below the metastable critical thickness. Fortunately, the experimentally feasible dislocation-free layer thicknesses are still wide enough to accommodate devices which are superior to conventional silicon based technology. A bonus of strained SiGe is that its band gap decreases faster with growing Ge content than in the unstrained material [85P]. This is due to the splitting and shifting of the bands under built-in compression as discussed in chapter V. Therefore, Ge contents of only 20-30 % are needed for many electronic applications.

II.D.1.Quantum Wells

A quantum well (QW) is a heterostructure of pseudomorphically grown alloy layers. The band alignment of the alloys is chosen in such a manner, that the CBs and VBs form an energy well in one or several layers. Excited charge carriers diffuse through the heterostructure until they are confined to their

corresponding potential wells, forming 2-D gases. As discussed in the introduction, a pseudomorphically grown Si/SiGe/Si QW forms a hole well in the SiGe, but the nature of the small discontinuity at the CB is still unresolved.

II.E. Motivation for this study

This section gives an overview of existing Si/SiGe based technology. The question as to the band alignment of the Si/SiGe interface is not merely of academic interest as it is a major consideration in the design of SiGe based devices. The exact knowledge of the band alignment allows a common doping technique, called *modulation doping,* to be implemented. In this method, thermalized charge carriers can be decoupled from their ionized impurities by forcing them into the potential well of an adjacent layer [84D]. This technique renders faster devices and has already been successfully implemented in bipolar transistors using SiGe bases with twice the speed of conventional Si homojunction devices [90P], [95M], [95S]. In these transistors the holes from the p-doped Si emitter and collector are trapped in the SiGe well where interaction with the ionized acceptors is reduced. The resulting 2-D hole gas has exhibited mobilities of 3300 $cm^2V^{-1}s^{-1}$ [84P]. In comparison with GaAs based alternatives, the technical advantage of these heterojunction bipolar transistors (HBT) is their compatibility with existing Si based circuits.

Other applications include the production of light emitters by building neighboring confinement structures (NCS). For optical applications, it is

necessary to confine both electrons and holes between high potential barriers. Since in an NCS device, a tensile-strained Si and a compressed $Si_{1-x}Ge_x$ layer are sandwiched between relaxed $Si_{1-y}Ge_y$ ($x>y$), induced electrons and holes are confined in the Si and $Si_{1-x}Ge_x$ potential wells, respectively [85A], [95U]. At an optimized Si layer width, this structure yields an enhanced SiGe no phonon PL line in comparison to a single SiGe QW. This increased transition probability in thin confining layers is attributed to the tunneling of the spatially separated electron and hole wave-functions into the neighboring layer so that spatially direct transitions become possible [94M].

II.F. Past experimental and theoretical attempts to determine Δ_c

The following section gives a short account of past attempts to determine Δ_C. The fundamental problem of theoretically deriving the band lineups at a heterojunction is the absence of an internal reference energy in a bulk solid. This is due to long-range Coulomb interaction in an infinite bulk solid [86vdW]. Van de Walle and Martin tried to overcome this problem by carrying out self consistent *ab initio* local density calculations of a superlattice [86vdW]. The unit cell of this 1-D superlattice was composed of 4 Si and 4 Ge atoms in series. The resulting potential averages in the Si and the Ge yielded reference energy levels in the two materials. The CB and VB levels can be calculated relative to these levels and hence the band alignment can be predicted. Van de Walle and Martin used

ab initio pseudo potentials and found a large Δ_V and a type I band alignment in $Si_{0.7}Ge_{0.3}$ on Si (001). Riegler and Vogl used the energy difference of the reference levels of L. Colombo *et al.* [91C] and subsequently found a type II band alignment, based on empirical pseudopotential calculations [93R]. In both models, the size of the Δ_C was in the order of tenths of meV compared to ~200 meV for Δ_V. People and Bean combined the calculated Δ_V of van de Walle and Martin with an experimentally determined value for the band gap of bulk SiGe and deformation potential theory to predict a type I interface [85P2].

The theoretical uncertainty in calculating the band alignment is compounded by the difficulty in confirming band discontinuities experimentally. Northrop *et al.* investigated the influence of hydrostatic pressure on the near-gap PL of SiGe QWs [92N] and concluded a type I band alignment. Fukatsu *et al.* recorded PL spectra from a coupled double QW (CDQW), that consisted of two SiGe QWs grown on bulk Si and separated by a Si layer of varying thickness. This thickness determines the extent of coupling between the layers. This study proposed a type I band alignment. Wachter *et al.* investigated the intensity of the PL signal as a function of excitation power and found two linear regimes with different slopes [92W]. For higher excitation powers, the signal intensity was found to grow faster than for lower. They argued that for high intensities charge accumulation of the well-confined holes caused a bending down of the CB and VB in the SiGe. In a type II interface, this would permit leakage of the hole wave functions into the Si, leading to a larger overlap of the hole and electron wave

functions. On the other hand, in a type I interface where the electrons are located in the SiGe, band bending would not be expected to influence the recombination probability. The same group used a Hartree Fock model to quantify the amount of band bending as a function of excitation density. They further recorded PL spectra of single and multiple SiGe QWs with varying well thickness and detected a slight energy upshift of the SiGe NP peak with increasing well width. This supported a type II alignment according to their model [94B]. In another paper, they investigated the energy dependence of SiGe PL under [001] compression for intermediate excitation power densities (100 $mWcm^{-2}$) [94M1]. They found an energy upshift of the PL signal, expected for type I PL, but did not explicitly draw any conclusion from this. Houghton *et al.* repeated their stress experiment with strain along the [110] and [100] directions. They also found an energy upshift for uniaxial tensile strain and using deformation potential theory correctly interpreted this as evidence of type I behavior [95H].

How can this confusion be resolved? Theory does not seem capable of determining the sign of Δ_C. This is certainly due to its small size as well as to uncertainties in the crucial difference between the reference levels in Si and SiGe. The experiment of Houghton *et al.* seemed very promising since it was only based on well-established deformation potential theory which, in the case of a type I or type II band alignment, yields opposing energy shifts of the SiGe PL under strain. Unfortunately, they neglected the important effect of band bending

under increasing excitation power, so that the physical picture remained incomplete.

II.G.Summary

Traditionally, silicon is the dominant semiconductor in electronic devices. To narrow its material-inherent limitations, strained SiGe layers can be pseudomorphically grown into existing silicon based devices. This growing mode avoids misfit dislocations at heterojunction interfaces and produces smaller alloy band gaps than in unstrained SiGe. Modulation doping has already lead to HBTs that outperform conventional silicon homojuntion devices.

III.Excitons and Photoluminescence in a Si/SiGe Quantum well

In this study, photoluminescence (PL) spectroscopy has been used to define the band alignment of the $Si/Si_{0.7}Ge_{0.3}$ interface. This section describes the physics of PL and its usage as a characterization tool.

III.A. Excitons and Photoluminescence

If above-band gap light is absorbed in a semiconductor, electrons are lifted from the VB to the CB, leaving holes behind. These holes can be treated like particles of positive unit charge and effective mass m_h^*. The excited electrons and holes interact with the crystal lattice and thermalize non-radiatively to the band edges of the CB and VB, respectively. After a material-specific lifetime (for SiGe from ns to ms), some pairs recombine radiatively. *Photoluminesence* (PL) is the light that is emitted due to electron-hole recombination. For sufficiently long lifetimes and excitation densities, an electron and a hole can be spatially bound *via* the Coulomb interaction before they recombine. They form a two-particle structure that resembles a hydrogen atom with the hole substituting as the proton. These structures are called *free excitons* (FE) and their binding energies are around 4 meV in Ge and 15 meV in Si. Excitons have to be studied in a cyrogenic environment since their binding

energies are much smaller than kT at room temperature (29 meV). Free excitons move freely in their host semiconductor adopting a Maxwell-Boltzmann distribution. The resulting PL transition energies are:

$$E_{photon} = E_{gap} - E_{binding} + K.E.$$

Ergo, a FE PL-line is sharp at the low energy side with a high energy Boltzmann tail. These lines obviously sharpen up with decreasing temperature. Acceptor and donor impurities act as potential wells which can attract one or several excitons and localize them. The resulting structures are called bound excitons (BE) and bound multiple exciton complexes (BMEC). The center of mass of BEs has zero kinetic energy since they are localized, hence they have sharp PL lines. BE transitions can be observed at low illumination densities and their binding energies are impurity-specific. At higher excitation powers the BE states saturate and PL spectra become dominated by FE transitions.

In indirect semiconductors, radiative recombination is normally assisted by the absorption or emission of a momentum-conserving phonon. At low temperatures, only the latter case is observed in PL spectra, generating lines that are called *phonon replicas*. They are downshifted from their no-phonon (NP) transition energies by their respective phonon energies. The existence of a NP line in an indirect semiconductor is due to the localization of the BE near its binding impurity. High localization in direct space corresponds to diffusiveness of the electron and hole wave functions in reciprocal space. The wave-functions

overlap in reciprocal space and thus permit direct transitions that conserve the crystal momentum [89Wb].

III.B. Photoluminescence in relaxed SiGe

Weber and Alonso have recorded PL spectra over the entire composition range of unstrained $Si_{1-x}Ge_x$ [89Wb]. Near band-edge low temperature PL spectra in Si and Ge are dominated by the optical recombination of BEs. Due to the indirect nature of Si, Ge, and SiGe, TA and TO (transverse acoustic/optical) phonon replicas are also present. Weber and Alonso found the TO (transverse optical 58 meV) replica to be the largest feature in a pure Si PL spectrum. For growing Ge content, x, the NP line was enhanced and became the largest feature in the spectrum. Glaser *et al.* [92G] explained the existence of the large NP peak in terms of a breakdown of the translational symmetry in the SiGe alloy. The momentum conservation condition is relaxed due to statistical variations of the Ge density in the alloy which leads to alloy scattering. The presence of Ge splits the Si TO line into three peaks. These peaks have been assigned by Weber and Alonso to be TO phonon replicas arising from lattice vibrations of nearest neighbor atoms, namely: Si-Si, Si-Ge and Ge-Ge. The Si-Si and Ge-Ge modes have the TO phonon energies of the pure elements, 58 meV and 35.4 meV, while the Si-Ge mode has the energy of an oscillator with the reduced mass of the two elements (49 meV). Barker theoretically predicted the split of the TO phonon in SiGe and a gradual change of the TA line from TA_{Si} to TA_{Ge} [68B].

In fact, the TA phonon replica smoothly shifts in the SiGe PL with varying Ge content and, in the study of Weber and Alonso, became the largest feature in the PL spectrum of pure Ge. The relative intensities of the three TO PL peaks in the SiGe change with Ge content and reflect the relative number of nearest neighbors (Si-Si, Si-Ge, Ge-Ge) if a random lattice-site occupation is assumed [89Wb]. This observation supports the random occupation of the elements in SiGe. The relative strength of the TA replica relative to that of the TO is discussed in VI. The FWHM (full width half maximum) of the NP line of unstrained SiGe is around 4 meV compared to less than 0.1 meV in pure Si and Ge. This signal broadening in the alloy is again attributed to spatial fluctuations in the Ge content [91S].

III.C. Photoluminescence in strained SiGe

The near-gap PL of fully strained SiGe quantum wells has been investigated by numerous groups. [91R], [92S], [92V]. Above band gap photons are absorbed in the SiGe and the Si and the resulting holes diffuse into the SiGe potential well. J. Spitzer *et al.* achieved a NP FWHM of about about 5 meV which compares well with the resolution attained in unstrained SiGe[92S]. The quality of fully strained SiGe on Si has improved since then and NP FWHMs of only 1.5 meV have been reported by Lafontaine *et al* [96L]. After accounting for the relevant energy shifts due to quantum confinement, spatially varying alloy

composition and strain, the spectra of fully strained SiGe/Si QWs coincide with the bulk spectra discussed above:

- Charge carriers in a QW are subject to a finite square well potential, i.e. they are spatially confined by an energy barrier. Hole confinement in Si/SiGe QWs is more effective due to the large Δ_V which results in decreasing radiative transition energies (i.e. higher confinement energies) with increasing QW thickness.
- In some samples, low excitation PL spectra (<100 μWcm^{-2}) revealed the presence of localized excitons (LE) [92L], [93L]. These excitons localize in regions of above-average Ge content in the alloy. LEs exhibit unusual long lifetimes of up to 0.7 ms. This is due to reduced Auger recombination for the LEs compared to BEs. Above illumination powers of 100 μWcm^{-2}, all LE wells become filled and their signal saturates, so that the still growing BE signal hides their presence in the PL spectra. In turn, the FE signal dominates over the BE signal upon further increasing illumination power.
- The effect of strain on the PL of commensurate SiGe on Si is described by deformation potential theory in section V.

In samples with dislocations at the interface, a series of broad luminescence bands appears below the SiGe PL. The bands are completely suppressed in high quality samples, indicating a dislocation-free growth.

III.D. Summary

Near gap PL spectroscopy is a popular characterization technique which can be used to detect the presence of impurities and to monitor the change of the band gap in a semiconductor. The PL spectra of fully strained SiGe on Si show principally the same features as the unstrained bulk material which indicates that these heterostructures can be grown without dislocations at the interface. Sharp near-gap PL of SiGe demonstrates the high sample quality, and has been used to study the physics of the Si/SiGe interface.

IV. Experimental Techniques

The standard components in a system to study low temperature photoluminescence are a dewar, an excitation source, a spectral analyzer and a detector. In the case of stress studies, a bending rig must also be included. The SiGe luminescence falls between the Si and Ge band gap, i.e. roughly between 1.63 μm and 1.06 μm. The PL spectra discussed in this thesis have been recorded using both Fourier transform and dispersive spectrometers.

IV.A.Samples

The investigated samples were grown by H. Lafontaine at the National Research Council of Canada (NRC) in Ottawa. They were cleaved from a wafer upon which a 30 Å $Si_{0.7}Ge_{0.3}$ single quantum well was pseudomorphically grown on (001)Si and capped with a 1000 Å Si layer by ultra-high vacuum chemical vapor deposition (UHV-CVD) [96L]. UHV-CVD was first introduced by Meyerson in the mid-eighties [86M], [94C]. It is essentially a conventional CVD system in a ultra-high vacuum environment (~10^{-9} mbar) and growth temperatures for SiGe in the neighborhood of 525 °C. Generally, the substrate surfaces are cleaned *ex-situ* using an $HF:H_2O$ (1:10) dip for ~10s to remove C and O impurities. The resulting thin hydrogen surface layer is removed at elevated growing temperatures. The deposition reaction is an equilibrium process of silane (SiH_4) absorption and H_2 desorption [94C]. The SiH_4 sticks to the surface and

decomposes to Si and $2H_2$. The relatively low growth temperatures still allow for deposition rates of ~20 - 50 Å/min, while keeping impurity diffusion sufficiently low for device production. The benefit of working at low pressures is the suppressed conversion of silane into the radical silylene (SiH_2). This radical sticks to the surface and prevents further growth, leading to film inhomogeneity. The *"strengths"* of UHV-CVD are the high sample throughput and the reproducible layer uniformity. In the NRC growth system, up to 25 6" wafers can be grown simultaneously since the reduced deposition temperature results in a low silane decomposition coefficient. The carrier gases can flow uniformly throughout the chamber resulting in homogeneous epitaxy. [96L]. Si/SiGe interfaces are created by changing the composition of the hydride source gases (SiH_4, GeH_4, B_2H_3, etc.). Sharp commensurate interfaces can be generated since misfit dislocations are frozen out. The growth rate rises with increasing Ge content since the weaker Ge-H bond relative to H-Si promotes hydrogen desorption from the surface. Above ~25% Germanium content, the growth rate stabilizes at 50 Å/min. At this composition, the differences between the GeH_4 and SiH_4 sticking probabilities compensate the enhanced hydrogen desorption [91R1]. The major disadvantage of UHV-CVD is the relatively low growth rate compared to the 300 Å./min. typically achieved with MBE systems. This limitation is overcome, however, by the high wafer quantity throughput, which makes it an attractive candidate for commercial applications [94C].

Wafer composition and crystal orientation can be determined by X-ray diffraction and Transmission Electron Microscopy. In the system in which our sample wafer was grown, a composition uniformity as high as ±0.15% across a waver has been achieved [96L].

IV.B.Excitation source

We used an Ar^+ ion laser for PL excitation. The laser light is absorbed in the Si as well as in the SiGe QW. As a result, our recorded PL spectra are a superposition of luminescence from both Si and SiGe. The former was used as an internal calibration of the applied stresses. The strain dependence of the Si PL is calculated in section V following a paper by Laude and Cardona [71L]. The excitation power density was changed over 8 orders of magnitude (from 10 Wcm^{-2} to 100 $nWcm^{-2}$). To cover this very wide range, a set of neutral density (ND) filters were employed. In some power regimes, the PL spectra change drastically with illumination power. To suppress noise in the signal due to excitation power density variations, the laser light was fed into a LiCONiX (Model 50SA) stabilization accessory before illuminating the sample. The key component in this device is an acousto-optic modulator, which is a glass medium in which a refractive index grating is established by a piezoelectric transducer driven by radio-frequency power. The incident light is split into zeroth and first order Bragg beams. Depending on the configuration of the device, either the

zeroth or the first order Bragg beams are discarded afterwards. Before leaving the device, the transmitted beam looses some 4% of its intensity at a beam splitter. The retained 4% of the light are collected by a photodiode and the generated current is compared to a calibrated reference current. The difference between the two currents is fed into the feedback loop which controls the accousto-optic modulator and hence stabilizes the intensity of the laser beam.

IV.C. Dewar

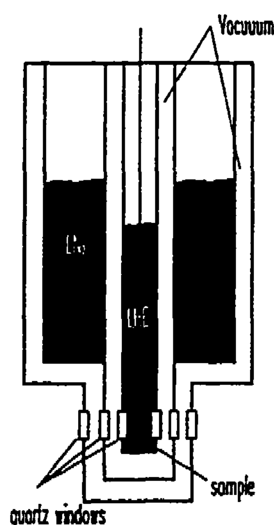

The purpose of the dewar is to keep the samples at sufficiently low temperature in order to perform near band PL of the Si/SiGe heterostructure. A dewar is composed of an inner sample chamber filled with liquid He, that is pumped below the λ–point (~1.6K) to lower the temperature and exclude the presence of He gas bubbles that could scatter the signal PL. The sample chamber is shielded from the 300 K world by a vacuum chamber, a liquid nitrogen chamber and a second vacuum chamber, both at <10^{-6} Torr. The liquid nitrogen jacket ends above the tail of the dewar. In the tail, sets of quartz windows allow both excitation and signal collection. Schott KG5 IR blocking filters were inserted before the excitation window of the dewar to prevent IR radiation from entering the tail.

These filters are heat absorbing glasses that only transmit visible light, i.e. the excitation laser light.

The samples were subject to external stress. The utilized bending-rigs were immersed in liquid He and could be externally operated from the top of the dewar by gliding metal rods. This heat conducting bridge was the major loss of liquid He during low light level experiments.

For low excitation measurements (100 $nWcm^{-2}$ to 10 μWcm^{-2}) , we used both dispersive and Fourier transform spectroscopy to collect two sets of spectra. This was necessary to fix the otherwise uncalibrated dispersive results. At higher illuminations, we only used the Fourier transform collection mode, since it allowed us to obtain higher resolution (0.5 cm^{-1}) spectra. This was useful to precisely determine the position of the Si TO replica and hence the magnitude of the applied external strain.

IV.D. Strain Geometries

Strain dependent PL spectra from two different geometrical setups have been recorded.

IV.D.1. Uniaxial stress along [110]:

In the uniaxial geometry the wafer was cut into 1 cm wide and ~5 cm long rectangular pieces aligned along the [110] direction. The sample was held fixed at one end and a mechanical arm bent down the free end (Fig. IV-1 (a)). This

caused an uniaxial tensile stress in the epilayer, oriented along the [110] direction. Unfortunately, this bending configuration only supported pressures up to 90 MPa before the sample broke. The experimental challenge was to vary the strain in the cold, brittle sample without breaking it.

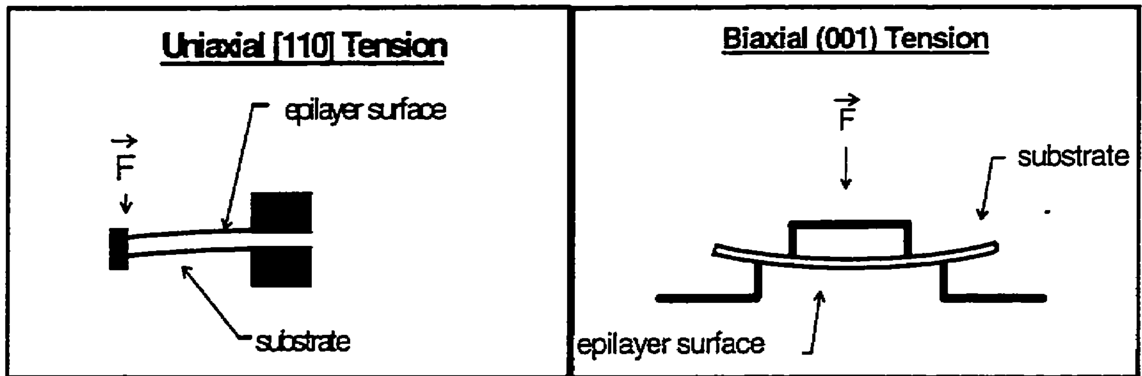

Figure IV-1: Schematic from the side of the uniaxial [110] and biaxial (001) bending rigs (a) In the biaxial bending rig the rectangular samples are cut along the [110] direction and a mechanical force presses down on the free end. (b) The circular samples are inserted between two concentric rings of different diameters, which are pressed together.

IV.D.2. Biaxial Geometry in the (001) plane

Placing a large-area, circular sample (~5 cm^2) between two concentric rings of different diameters (1.2 cm and 2.4 cm) which are forced together, generates a uniform biaxial strain (Fig. IV-1(b)). This bending configuration has been successfully used on GaAs, before, [96H] and produces remarkably uniform biaxial strain across the sample which becomes evident in the spectra. The FWHM of the SiGe peaks varied from 5.6 meV for zero stress to 11 meV

under high power conditions and 220 MPa of tension. These results compare well with the best obtained resolution in externally unstrained material [93L].

IV.E. Spectral Analyzer and Detector

The bulk of the PL spectra presented in this thesis have been collected using a Fourier transform spectrometer while a grating spectrometer was employed during the lowest excitation conditions.

IV.E.1. Fourier Transform Spectroscopy

Fourier Transform spectroscopy has been carried out using a Bomem DA8 interferometer in combination with a Northcoast single Ge detector at 77K. As schematically described in Fig. IV-2, the Bomem is based on a Michelson interferometer.

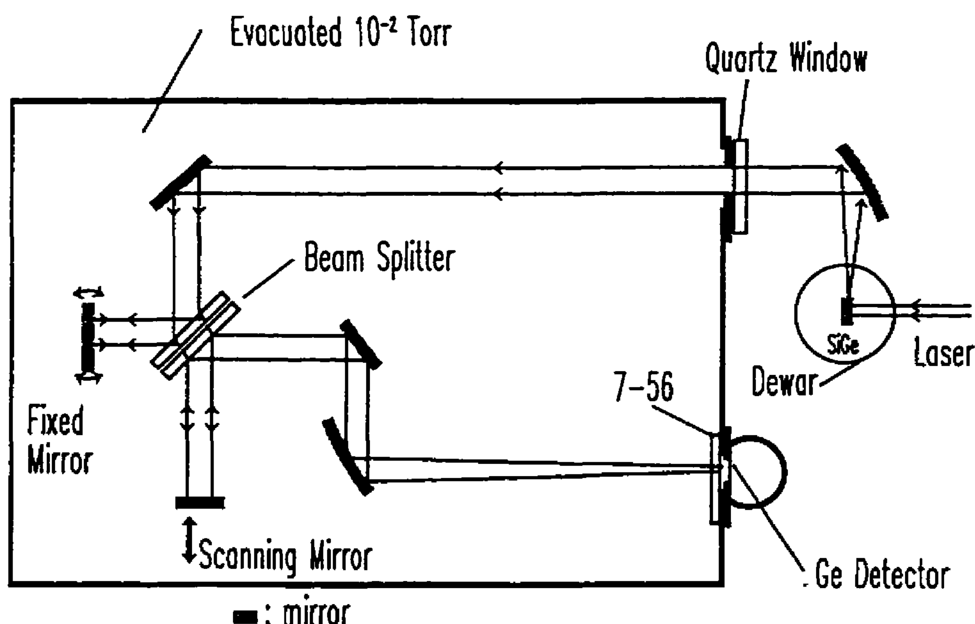

Figure IV-2: Configuration for the Fourier Transform Spectroscopy

The signal enters the interferometer through an quartz window and is split by a quartz beam splitter (BS). The partially reflected and partially transmitted beams reflect at the fixed and the scanning mirror, respectively, and recombine phaseshifted at the BS before leaving the interferometer. In operation, the moving mirror is driven at a constant velocity and the varying differences of the optical path length, x, lead to interference between the different wavelengths. The resulting signal has an intensity:

(IV-1) $$I(x) = 2\int_0^{\infty} S(\lambda^{-1})\cos\left(\frac{2\pi x}{\lambda}\right)d\left(\lambda^{-1}\right)$$

where $S(\lambda^{-1})$ is the spectral density of the signal. The inverse Fourier transform of equation (IV-1) is:

(IV-2) $$S(\lambda^{-1}) = 2\int_0^{\infty} I(x)\cos\left(\frac{2\pi x}{\lambda}\right)d(x)$$

The intensity of the signal leaving the interferometer I(x) is recorded as a function of the path length difference and used to calculate the signal spectrum. Since the range of x is experimentally limited, the signal spectrum can be obtained up to a resolution of 0.02 cm^{-1} in the Bomem DA8 [BM]. This remarkably high resolution requires several features of the Bomem:

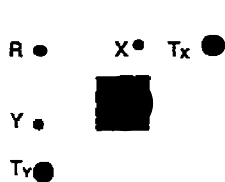

- Dynamic alignment of the fixed mirror: The fixed and the scanning mirror need to be kept parallel in order to avoid optical path differences of the signal across the collimated beam. For *in situ* alignment, the light of an internal HeNe laser is split in three focused and two unfocused beams that are arranged as shown in

the inset above (R, X, Y focused, T_x, T_y unfocused). The interferograms of X, R and Y are collected by photodiodes and a relative phase change between R and X (Y) indicates a tilt in the X (Y) direction. The unfocussed beams have to be employed when the two mirrors are strongly misaligned. The detected tilts are corrected by two servomotors with up to 2000 degrees of phase changes/sec. The five Laser beams are accompanied by a beam of white light (black square in the Figure). White light has a very short coherence length so that it can only constructively interfere for zero path length difference (ZPD). Hence, a peak in the signal of a photodiode that monitors the intensity of the white light interferogram marks the ZPD point (zero path length difference).

- Light of different wavelengths have different velocities in the BS material. This introduces an additional phase shift between the signals from different wavelengths. To suppress this phase shift, the BS of the Bomem is composed of two equally thick, parallel, polished single quartz crystals. They are reflectively covered on the inner surfaces. As schematically shown in Fig. IV-2, the transmitted and reflected beams travel the same distance through the BS. The remaining optical path difference is due to thickness variations between the two BS plates which are kept below ±0.01 mm [BM].

The detector, used in combination with the Bomem, was a liquid-nitrogen-cooled Ge-photodiode (Northcoast). The electronic signal from the detector was amplified before entering a computer for Fourier analysis. Any light from the Ar^+ laser, that scattered into the PL signal, was attenuated by an infrared

transmitting, visible absorbing, Corning 7-56 filter with a cut-off energy at ~0.75 μm.

IV.E.2. Dispersive Spectroscopy

In our dispersive system, the PL signal was passed through a 7-56 absorptive glass filter to exclude any scattered laser light before it entered the dry-air-purged SPEX monochromator through a 0.25 mm wide slit. The signal was dispersed by a 300 g/mm grating and the SiGe spectra between 1.5 μm and 1.3 μm was collected by a linear 128-Element Ge Photodiode Array (EG&G Judson J16M). We operated at a resolution of ~9 cm^{-1}.

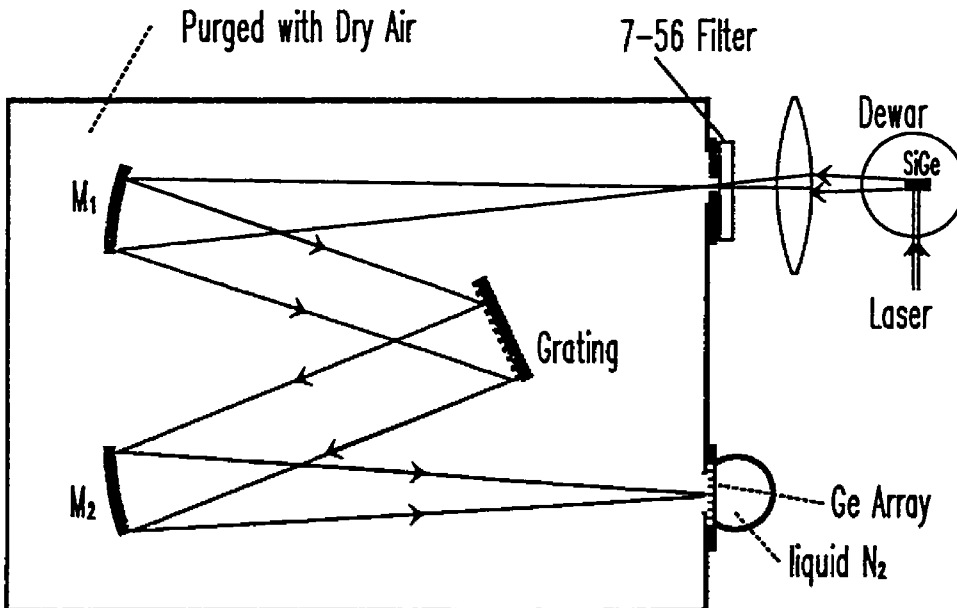

Figure IV-3: Configuration of the Dispersive Spectrometer

IV.E.3. Comparison between Dispersive and Fourier Transform Spectroscopy

A conceptual disadvantage of dispersive spectroscopy is that the PL signal is restricted to enter the spectrometer through a 0.25 mm wide slit in order to obtain sufficient resolution, while in the Bomen the signal enters through a 1 cm (diameter) aperture. This is called the *"throughput advantage"* of interferometers over grating spectrometers.

Further, a Fourier transform spectrometer collects the entire energy spectrum simultaneously with a single detector. In comparison, a single detector is limited to record one spectral channel at a time in a dispersive setup. Traditionally, this had lead to the *"multiplex advantage"* of interferometers over grating spectrometers. With the introduction of linear Ge-arrays, which simultaneously record a fixed spectral region of interest, this short-coming of dispersive spectroscopy has been somewhat overcome. In our setup, the Ge array exclusively detects the SiGe luminescence and is capable of detecting PL from illumination intensities as low as 10^{-8} Wcm^{-2}. For reasonable measurement times, such weak signals are several orders of magnitude below the detection limit of the Bomem.

IV.F. Time-resolved Photoluminescence

To measure the lifetimes of the excitons in SiGe, the laser excitation was chopped at 200 Hz. The integrated SiGe PL signal, recorded by the Ge detector

was fed into an oscillograph. When the laser light was blocked, the observed signal decayed exponentially with a characteristic decay-time corresponding to the lifetime of the excitons.

IV.G. Procedure

PL spectra from a $Si/Si_{0.7}Ge_{0.3}$ single QW have been recorded under a wide range of illumination powers and two strain geometries. The magnitude of the external stress on the sample was internally calibrated by measuring the line shift of the boron BE TO phonon replica from the silicon substrate. The stress in the alloy layer and the top of the substrate were assumed to be identical, since the QW was only 30 Å wide. To measure the lifetimes of the excitons, time resolved PL was performed for a range of stresses and excitation power densities.

V.Photoluminescence Spectra under Strain

In this section, a model is developed to quantify the effect of external strain on the SiGe and Si PL features. We have used deformation potential theory to calculate the shifting and splitting of the CBs and VBs under strain. Our calculations reveal distinguishable behaviors for type I and type II band alignments at the interface. Our analysis follows the work of Laude, Pollack and Cardona [71L], who calculated the effect of external stress on the CBs and VBs in Si. We generalize their model to account for a SiGe QW under both uniaxial [110] and biaxial (001) tensions.

The energy of a SiGe BE NP line depends on the exciton binding energy, which is small and relatively constant, and on the energy difference between the CB and VB edges. Depending on whether the band alignment is type I or type II, electrons will be confined in the SiGe or Si and recombine with holes in the SiGe (Fig. V-1). According to Cardona *et al.* [71L], changes of the exciton binding energies are in the order of 4 cm^{-1} under external stresses below 1 GPa. We can neglect these effects, since the highest stresses obtained were 220 MPa before our samples broke. Within this approximation the shift of the NP peak exactly reflects the relative shifts of the relevant CBs and VBs.

We proceed in several steps: First the applied external stresses have to be transformed into strain (section V.A). In sections V.B and V.C, the Kleiner-Roth, Hering-Vogt and hydrostatic deformation Hamiltonians are identified and solved for the two bending configurations.

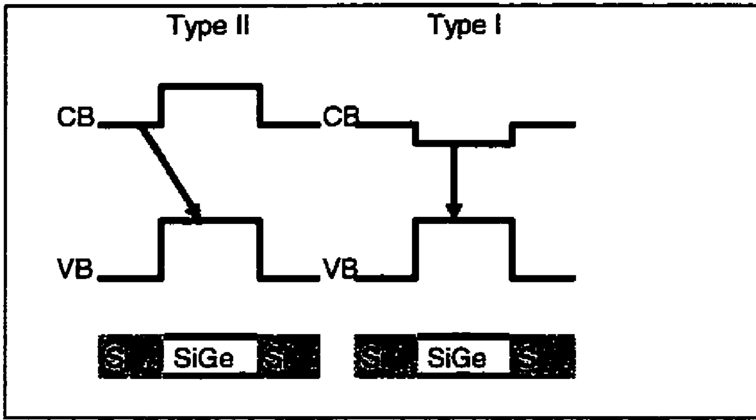

Figure V-1: *Transitions due to type I and type II band alignments.*

V.A. From Stress to Strain

V.A.1. Stress

An external force, $\bar{F}$, acting on the surface of a body deforms it. *Stress*, σ, is the physical quantity that describes the balancing internal action and reaction between different parts of a body. It specifies the force per unit area at any point of the body across any plane. Accordingly, stress is measured in units of pressure and can be represented by a (3x3) matrix which generally varies throughout the body [1892L]. Our bending-rigs produced a uniform uniaxial or biaxial stress throughout the illuminated region of the sample, i.e. $\sigma(r)=\sigma$. The matrix elements are basis-dependent and for any unit vector, $\bar{n}$, $\sigma\bar{n}$ yields the stress parallel to $\bar{n}$. σ_{ij} is symmetric, $\sigma_{ij}=\sigma_{ji}$, with six independent components. The stress elements, due to an external pressure , $\bar{P}$, are given by:

(V-1) $$\sigma_{ij} = |P| m_i m_j ,$$

where $\bar{m}$ is the unit vector parallel to $\bar{P}$.

V.A.2. Strain

How does stress relate to the deformation of a body? *Strain,* ε, is defined as the relative displacement of a point in a deformed body from its 'unstrained' position. Three shear and three normal components completely define a matrix that provides displacement from a point in the body in any direction. The *generalized Hook's Law* states that stress and strain are proportional, i.e. each of the six strain components is a linear function of the six stress components and *vice versa*. This approximation is only valid for the regime in which a deformed body recovers its original shape. It is a convenient mathematical notation to express stress and strain as 6-dimensional vectors, linked by (6x6)matrices, S and C:

(V-2) $$\bar{\varepsilon} = S\bar{\sigma}; \quad \bar{\sigma} = C\bar{\varepsilon}$$

The elastic constants (C) and the compliances (S) are material dependent. Fortunately, Si, Ge and SiGe are cubic crystals, therefore their matrices reduce to the simplified, symmetrized form [76H], [1892L]:

(V-3) $$S = \begin{pmatrix} s_{11} & s_{12} & s_{12} & & & \\ s_{12} & s_{11} & s_{12} & & 0 & \\ s_{12} & s_{12} & s_{11} & & & \\ & & & \frac{s_{44}}{2} & & \\ & 0 & & & \frac{s_{44}}{2} & \\ & & & & & \frac{s_{44}}{2} \end{pmatrix}^{*}$$

* The matrix C has the same reduced form for a cubic crystal, with $S_{ij} \mapsto C_{ij}$. Unfortunately, there exists some confusion about a factor 2 in the literature, so that one can find $s_{44}/4$ instead of $s_{44}/2$ in the matrix for S, where the ambiguity arises from different definitions of s_{44} [63H].

V.A.3. Strain in the two Bending Geometries

Now, we can link the applied stresses in both bending configurations to the strains in the sample.

• ***Built-in Strain in the $Si_{0.7}Ge_{0.3}$ Layer:***

A $Si_{0.7}Ge_{0.3}$ layer, pseudomorphically grown on bulk Si, is under internal uniform biaxial compression. The theory of elasticity is linear.Therefore built-in and external strains simply superimpose and can be treated independently. The strain components for the built-in strain in the x-y plane are given by their relative displacement from the unstrained shape:

(V-4) $$\varepsilon_{xx}^{in} = \varepsilon_{yy}^{in} = \frac{a_{Si} - a_{SiGe}}{a_{SiGe}} = \frac{a_{Si}}{a_{SiGe}} - 1 = \alpha,$$

where a_{Si} and a_{SiGe} are the lattice constants of the two materials. Since a_{Si}=5.431Å and a_{SiGe}=5.499Å (for 30% Ge) we find that α=-0.012. The in-plane compression forces the SiGe to expand perpendicular to the plane in order to minimize its elastic energy at the interface. The magnitude of this expansion is given by Hooke's Law [94M] with σ_{zz}=0:

(V-5) $$\varepsilon_{zz}^{in} = -\frac{2c_{12}}{c_{11}}\varepsilon_{xx}^{in} = \left(\frac{2s_{12}}{s_{11}+s_{12}}\right)\varepsilon_{xx}^{in}\ ^{*}$$

All shear components are zero, as can be seen in Fig. V-2., which illustrates the deformation of the Si and SiGe cubic lattices for both bending geometries. The dotted lines represent the undeformed unit cells while the solid lines show the

* The relationship between c_{ij} and s_{ij} was taken from [72B]. The coefficients, c_{ij} are the *elastic constants* which are defined by: $C\bar{\varepsilon} = \bar{\sigma}$

unit cells after deformation. The non-zero strain components are shown together with their associated deformation directions. Fig. V-2 (a) shows that internal strain leaves the Si substrate undeformed, (i.e. there is no internal strain for the Si). In Fig. V-2 (b) we see that the SiGe unit cell acquires the lattice constant of Si parallel to the interface. The crystal symmetry reduces from cubic to tetragonal.

• ***Uniaxial [110] Stress :***

For a force along the [110] direction, the strain is given according to eqn V-1:

(V-6) $$\vec{\sigma} = \begin{pmatrix} \sigma_{xx} \\ \sigma_{yy} \\ \sigma_{zz} \\ \sigma_{yx} \\ \sigma_{yz} \\ \sigma_{xz} \end{pmatrix} = T \begin{pmatrix} n_x n_x \\ n_y n_y \\ n_z n_z \\ n_x n_y \\ n_y n_z \\ n_x n_z \end{pmatrix} = \frac{T}{2} \begin{pmatrix} 1 \\ 1 \\ 0 \\ 1 \\ 0 \\ 0 \end{pmatrix} \Rightarrow \vec{\varepsilon} = \begin{pmatrix} \varepsilon_{xx} \\ \varepsilon_{yy} \\ \varepsilon_{zz} \\ \varepsilon_{xy} \\ \varepsilon_{yz} \\ \varepsilon_{xz} \end{pmatrix} = S\vec{\sigma} = \frac{T}{2} \begin{pmatrix} s_{11} + s_{12} \\ s_{11} + s_{12} \\ 2s_{12} \\ s_{44}/2 \\ 0 \\ 0 \end{pmatrix}$$

Where T is the magnitude of the applied pressure, $|\vec{P}|$; positive T denotes tension; negative T describes compression and $\vec{n}$ is the unit vector along the pressure direction. The effect of [110] tension on Si and SiGe has been illustrated in Fig. V-1 (c) and (d). The symmetries of both lattices are reduced to base-centered orthorhombic.

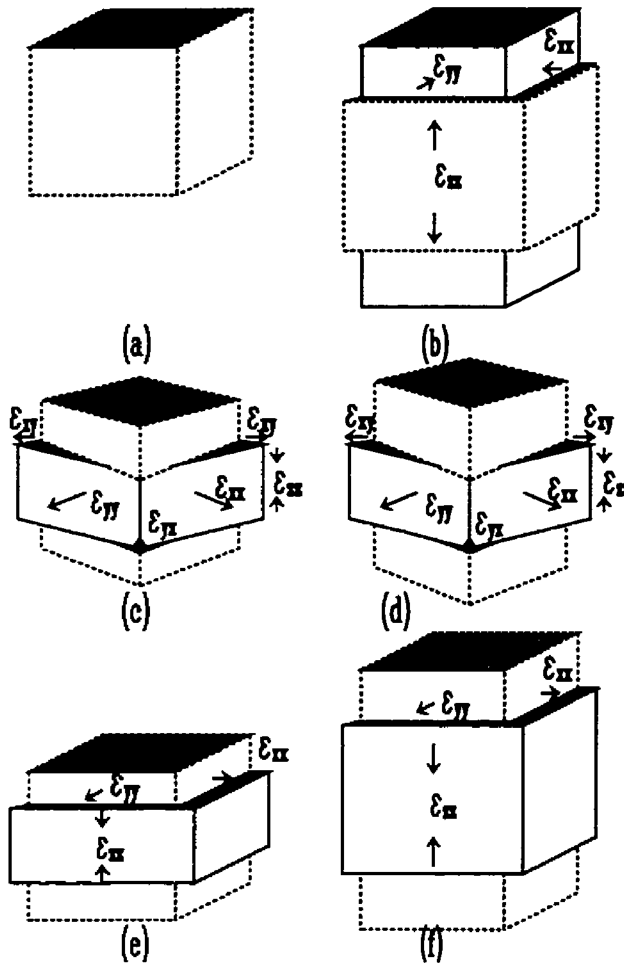

Figure V-2: *Effect of strain on the Si and SiGe lattices*

----undeformed ——deformed

built-in strain:
(a) the Si lattice is not affected because there is no built-in strain (the Si is very thick compared to the SiGe)

(b) the SiGe lattice symmetry reduces from cubic to tetragonal

uniaxial [110]:
(c) the Si lattice changes from cubic to base-centered orthorhombic

(d) the SiGe lattice reduces from tetragonal to base-centered orthorhombic

biaxial (001):
(e) the Si lattice reduces from cubic to tetragonal

(f) the SiGe lattice stays tetragonal and approaches cubic when the external stress exactly compensates the built-in strain

System	Restrictions on conventional cell axes and angles	
Triclinic	$a_1 \neq a_2 \neq a_3$	$\alpha \neq \beta \neq \gamma$
Monoclinic	$a_1 \neq a_2 \neq a_3$	$\alpha = \beta = 90^0 \neq \gamma$
Orthorhombic	$a_1 \neq a_2 \neq a_3$	$\alpha = \beta = \gamma = 90^0$
Base-Centered Orthorhombic	$a_1 = a_2 \neq a_3$	$\alpha ,\ \beta \neq \gamma = 90^0$
Tetragonal	$a_1 = a_2 \neq a_3$	$\alpha = \beta = \gamma = 90^0$
Rombohedral	$a_1 = a_2 = a_3$	$\alpha \neq \beta \neq \gamma$
Cubic	$a_1 = a_2 = a_3$	$\alpha = \beta = \gamma = 90^0$

Table V-1: *Three dimensional lattice types [53K],[69C]*

- ***Biaxial Stress:***

Apart from being tensile and not compressive, strain due to biaxial tension has the same geometry as the built-in strain treated above. It deforms both the Si and the SiGe as evident in Fig. V-2 (e) and (f) respectively. As a consequence, the cubic Si lattice becomes tetragonal. The SiGe lattice, while remaining tetragonal, moves closer to cubic symmetry. In analogy to the built-in strain, the shear components are zero and $\varepsilon_{xx}=\varepsilon_{yy}$. With $\sigma_{zz}=0$:

(V-7) $$\varepsilon_{xx}^{ex} = \varepsilon_{yy}^{ex} = (s_{11} + s_{12})T$$

(V-8) $$\varepsilon_{zz}^{ex} = -2\frac{c_{21}}{c_{11}}\varepsilon_{xx}^{ex} = \left(\frac{2s_{12}}{s_{11}+s_{12}}\right)\varepsilon_{xx}^{ex}$$

The upper formula describes the uniform strain within the xy-plane, while the second formula states that the elastic-energy-compensating strain along the z-axis is linked to the in-plane strain by the Poisson ratio for this geometrical setup. Fig. V-2(f) also reveals that for a single biaxial strain, external and build-in strain completely cancel each other.

Table (V-2) summarizes the strain components for the two bending geometries and presents the utilized values for the compliances s_{ij} taken from Brantley [72B]. Following a paper from van de Walle [86vdW], the values for $Si_{0.7}Ge_{0.3}$ were linearly interpolated from the given values for Si and Ge.

	Si	$Si_{0.7}Ge_{0.3}$
uniaxial tension along [110]	$\varepsilon_{xx}=\varepsilon_{yy}=(s_{11}+s_{12})\frac{1}{2}T$ $\varepsilon_{zz}=s_{12}T$ $\varepsilon_{xy}=s_{44}\frac{1}{4}T$ $\varepsilon_{xz}=\varepsilon_{zy}=0$	$\varepsilon_{xx}=\varepsilon_{yy}=(s_{11}+s_{12})\frac{1}{2}T$ $\varepsilon_{zz}=s_{12}T$ $\varepsilon_{xy}=s_{44}\frac{1}{4}T$ $\varepsilon_{xz}=\varepsilon_{zy}=0$
biaxial tension in the <001> plane	$\varepsilon_{xx}=\varepsilon_{yy}=(s_{11}+s_{12})T$ $\varepsilon_{zz}=2s_{12}/(s_{11}+s_{12})\varepsilon_{xx}$ $\varepsilon_{xz}=\varepsilon_{zy}=\varepsilon_{xy}=0$	$\varepsilon_{xx}=\varepsilon_{yy}=(s_{11}+s_{12})T$ $\varepsilon_{zz}=2s_{12}/(s_{11}+s_{12})\varepsilon_{xx}$ $\varepsilon_{xz}=\varepsilon_{zy}=\varepsilon_{xy}=0$
built-in stress	$\varepsilon_{xx}=\varepsilon_{yy}=\varepsilon_{zz}=0$ $\varepsilon_{xz}=\varepsilon_{zy}=\varepsilon_{xy}=0$ (unstrained layer)	$\varepsilon_{xx}=\varepsilon_{yy}=\alpha$ $\varepsilon_{zz}=2s_{12}/(s_{11}+s_{12})\varepsilon_{xx}$ $\varepsilon_{xz}=\varepsilon_{zy}=\varepsilon_{xy}=0$
elastic compliances	$s_{11}=$ 0.768*10^{-12} cm^2/dyn[@] $s_{12}=$ -0.214*10^{-12} cm^2/dyn $s_{44}=$ 1.26 *10^{-12} cm^2/dyn	$s_{11}=$ 0.8268*10^{-12} cm^2/dyn $s_{12}=$ -0.228 *10^{-12} cm^2/dyn $s_{44}=$ 1.329 *10^{-12} cm^2/dyn

***Table V-2:** Strain components and compliances induced by uniaxial and biaxial strain for Si and $Si_{0.70}Ge_{0.3}$.. The elastic compliances are taken from Brantley [72B].*

V.B.The Effect of Strain on Energy Bands

Strain has two components that effect the band structure of a semiconductor: The hydrostatic component shifts the energy position of the center of mass of a band, while the directional strain component splits degenerate subbands. Deformation potential theory conventionally describes the

---

@ $1\frac{dyn}{cm^2}=0.1\,Pa$

VB splitting with the Kleiner-Roth Hamiltonian and the CB splitting with the Herring-Vogt Hamiltonian. Both Hamiltonians are phenomenological in nature.

V.B.1. Hydrostatic Deformation Potential

Hydrostatic strain shifts the center of mass energies of the CB and VB. It is linear with respect to the fractional volume change, $\frac{\Delta V_{strained}}{\Delta V_{relaxed}}=(\varepsilon_{xx}+\varepsilon_{yy}+\varepsilon_{zz})$, also called the *dilatation.* The energy shift of a band is the product of the applied dilatation and the band- and material-specific hydrostatic pressure coefficient, "a" for the VB and "E_1" for the CB:

(V-9) $$H_{hydrostatic} = (\mathrm{E}_1 - a)(\varepsilon_{xx} + \varepsilon_{yy} + \varepsilon_{zz}) = \Xi_1(\varepsilon_{xx} + \varepsilon_{yy} + \varepsilon_{zz})$$

E_1 and a are independent parameters. Experimentally, one can only measure the shift of the energy difference between two bands and therefore, only the difference of the contributions, Ξ_1, is known.

V.B.2. Valence Band Splitting

Without strain and spin-orbit interaction, the VBs in Si and SiGe are sixfold degenerate p-multiplets, consisting of three pairs of spin-up and spin-down states. The Hamiltonian that describes the splitting of the three CBs is the sum of the spin-orbit and Kleiner-Roth Hamiltonians.

(V-10.a) $H = H_{spin-orbit} + H_{KR}$

Spin-orbit coupling arises from the interaction between the VB holes and the electric field of the atomic nuclei. In the rest frame of the hole, a magnetic field due to the electric field appears and interacts with the intrinsic magnetic moment of the hole.

(V-10.b) $$H_{spin-orbit} = \frac{1}{4m_h^{*2}c^2}\frac{1}{R}\frac{dV(R)}{dR}\vec{S}\bullet\left[\vec{R}\times\vec{P}\right] = const.\vec{S}\bullet\vec{L}$$

H is naturally described in the $|J,m_J\rangle$ basis of the total angular momentum, J, of the hole, since the operator $\vec{S}\bullet\vec{L} = \frac{1}{2}\left(J^2 - L^2 - S^2\right)$ is diagonal in that basis [68P], [94S]. The spin-orbit Hamiltonian does not affect m_J. Therefore, we need only consider the three states with positive m_J.

$|3/2,3/2\rangle$ $|3/2,1/2\rangle$ $|1/2,1/2\rangle$

(V-10.c) $$H_{spin-orbit} = \begin{pmatrix} \frac{E_{so}}{3} & 0 & 0 \\ 0 & \frac{E_{so}}{3} & 0 \\ 0 & 0 & -\frac{2E_{so}}{3} \end{pmatrix}$$

The two J=3/2 pairs, called the *heavy* ($|3/2, 3/2\rangle$) and *light holes* ($|3/2, 1/2\rangle$), are degenerate at k=0 under zero strain. The lowest energy pair (J=1/2) is the *splitoff* band.

Shear strain lifts the degeneracy of the heavy and light holes, since the sp^3 tetrahedral bonding orbitals are different mixtures of orbitals with p_x, p_y and p_z character, (i.e. they have non-zero angular momentum, and external shear strain affects them differently). Conventionally, the linear orbital-strain interaction

is described by a phenomenological Hamiltonian, which was introduced from symmetry considerations by Kleiner and Roth [59K]. Unfortunately, they did not include an explicit derivation, but the Hamiltonian has been used by numerous authors since 1959 [86vdW], [68P], [63H]:

(V-11) $$H_{KR} = -3b\left[\sum_{i=x,y,z}\left(L_i^2 - \frac{1}{3}L^2\right)\varepsilon_{ii}\right] - \sqrt{3}d\left[\sum_{ij=xy,xz,yz}\{L_i L_j\}\varepsilon_{ij}\right]$$

The first term in the expression reduces the tetragonal symmetry of the crystal, since ε_{ii} affects the crystal lattice constants a_1, a_2 and a_3. The second term affects the orthorhombic symmetry, changing α, β and γ. **L** is the angular momentum operator and the ε_{ij}'s are the strain components of the applied bending geometry. b and d are the VB deformation potentials. The brackets {} denote the symmetrized product, {xy}= ½(xy+yx).

V.B.3. Conduction Band Splitting

The splitting of the CB is different in nature from that of the VB. In the absence of stress, Si and $Si_{0.7}Ge_{0.3}$ have six degenerate CB mimima ($|\Delta_1\rangle$) along the Δ–axis near X [85P]. Depending on their position in reciprocal space, directional strain affects the CB minima differently. Herring and Vogt proposed that the splitting of the CBs could be described by [71L], [56H]:

(V-12) $$\Delta E = \Xi_2 \vec{n} * [\varepsilon - \frac{1}{3}(\varepsilon_{xx} + \varepsilon_{yy} + \varepsilon_{zz})\bar{1}] * \vec{n}$$

where ε is the strain matrix $\varepsilon = \begin{pmatrix} \varepsilon_{xx} & \varepsilon_{xy} & \varepsilon_{xz} \\ \varepsilon_{yx} & \varepsilon_{yy} & \varepsilon_{yz} \\ \varepsilon_{zx} & \varepsilon_{zy} & \varepsilon_{zz} \end{pmatrix}$,

and $\bar{1}$ is the identity matrix and $\vec{n}$ is the unit vector in the direction of the critical point in k-space, i.e. the six <100> directions. Ξ_2 is the shear deformation potential which is considered to be equal in both layers, since there are no experimental values available for the <001> valleys in Ge. This approximation was justified by van der Walle, who obtained similar theoretical values for Ξ_2 in Si and Ge [86vdW]. Physically, the matrix $\varepsilon - \frac{1}{3}(\varepsilon_{xx} + \varepsilon_{yy} + \varepsilon_{zz})\bar{1}$ describes the directional component of the strain tensor, i.e. the dilation is subtracted from ε. Multiplication of the (3x3) matrices of the left and right by the 3-D vector $\vec{n}$ projects the directional component along the valley-direction of interest. This yields the magnitude of the strain, induced for this valley.

In the diamond structure, the six CBs, Δ_1, are degenerate with the six $\Delta_{2'}$ bands at the X point of the reciprocal lattice. In the presence of an orthorhombic distortion, a non-linear shift due to stress induced coupling between the Δ_1 and $\Delta_{2'}$ bands causes a second order repulsion [71L], [65H]. The following matrix describes the strain-induced splitting of the two bands along the [001] direction:

$$|\Delta_1\rangle \qquad |\Delta_{2'}\rangle$$

(V-13) $$\begin{pmatrix} 0 & 2\Xi_2^{*}\varepsilon_{XY} \\ 2\Xi_2^{*}\varepsilon_{XY} & E(\Delta_{2'}) - E(\Delta_1) \end{pmatrix}$$

Equivalent matrices for the other valleys are obtained by cyclic permutation of the x, y and z indices. The shift of the CB minima to second order in shear strain is given by the eigenvalue of (V-13):

(V-14) $$\delta E^{*(001)} = -\frac{(2\Xi_2^{*}\varepsilon_{xy})^2}{E(\Delta_{2'}) - E(\Delta_1)}$$

In unstrained Si, $E(\Delta_{2'})$-$E(\Delta_1)$ is equal to 0.8 eV. Again, we used the same values for the $Si_{0.7}Ge_{0.3}$. All other band couplings were neglected since relevant energies are sufficiently far apart [71L].

V.C. Calculation of the energy shifts

In this section we calculate and solve the strain Hamiltonians for the two bending geometries.

V.C.1. Biaxial Strain :

The non-zero strain components are $\varepsilon_{xx}=\varepsilon_{yy}$ and ε_{zz}. This simplifies the Kleiner-Roth Hamiltonian (eqn V-11) to:

(V-15) $$H_{KR} = -\frac{3}{2}\delta E_{001}\left(L_z^2 - \frac{L^2}{3}\right)$$

with $\delta E_{001} = 2b(\varepsilon_{zz} - \varepsilon_{xx}) = 2b(S_{12} - S_{11})T$

The total splitting of the CB is obtained by calculating the matrix elements of the Kleiner-Roth Hamiltonian in the $|J,m_J\rangle$ basis and adding them to the spin-orbit

matrix, eqn V-10.c [68P]. The effect of $L_z - \frac{L^2}{3}$ on the |J,m$_J$> basis is found by expressing the basis in terms of the direct product states, $|l,m_l> \otimes |s,m_s>$, of the eigenstates of the orbital angular momentum and spin of the holes:

(V-16) |J,m$_J$>= |l,m$_l$,s,m$_s$>

$$\left|\frac{3}{2},\frac{3}{2}\right\rangle = \left|1,1,\frac{1}{2},\frac{1}{2}\right\rangle \qquad \left|\frac{3}{2},-\frac{3}{2}\right\rangle = \left|1,-1,\frac{1}{2},-\frac{1}{2}\right\rangle$$

$$\left|\frac{3}{2},\frac{1}{2}\right\rangle = \sqrt{\frac{2}{3}}\left|1,0,\frac{1}{2},\frac{1}{2}\right\rangle + \sqrt{\frac{1}{3}}\left|1,1,\frac{1}{2},-\frac{1}{2}\right\rangle \qquad \left|\frac{3}{2},-\frac{1}{2}\right\rangle = \sqrt{\frac{1}{3}}\left|1,-1,\frac{1}{2},\frac{1}{2}\right\rangle + \sqrt{\frac{2}{3}}\left|1,0,\frac{1}{2},-\frac{1}{2}\right\rangle$$

$$\left|\frac{1}{2},\frac{1}{2}\right\rangle = -\sqrt{\frac{1}{3}}\left|1,0,\frac{1}{2},\frac{1}{2}\right\rangle + \sqrt{\frac{2}{3}}\left|1,1,\frac{1}{2},-\frac{1}{2}\right\rangle \qquad \left|\frac{1}{2},-\frac{1}{2}\right\rangle = -\sqrt{\frac{2}{3}}\left|1,-1,\frac{1}{2},\frac{1}{2}\right\rangle + \sqrt{\frac{1}{3}}\left|1,0,\frac{1}{2},-\frac{1}{2}\right\rangle$$

This yields:

|3/2,3/2> |3/2,1/2> |1/2,1/2>

(V-17)
$$H = H_{spin-orbit} + H_{KR} = \begin{pmatrix} \frac{E_{so}}{3} - \frac{\delta E_{001}}{2} & 0 & 0 \\ 0 & \frac{E_{so}}{3} + \frac{\delta E_{001}}{2} & \frac{\sqrt{2}}{2}\delta E_{001} \\ 0 & \frac{\sqrt{2}}{2}\delta E_{001} & -\frac{2E_{so}}{3} \end{pmatrix}$$

E_{so} is the spin-orbit splitting and has the value 0.44 eV for Si and 0.115 eV for $Si_{0.7}Ge_{0.3}$. The latter was obtained by linear interpolation between the Si and Ge values [85P]. The physical meaning of this matrix is that the light hole band, |3/2,1/2>, couples with the splitoff band , |1/2,1/2> and moves down in energy, while the heavy hole band moves up. The eigenenergies of the three subbands are:

(V-18.a) $$E_{heavy\ hole} = \frac{E_{so}}{3} - \frac{\delta E_{bi}}{2}$$

(V-18.b) $$E_{light\,hole} = -\frac{E_{so}}{6} + \frac{\delta E_{bi}}{4} + \frac{1}{2}\sqrt{E_{so}^{\ 2} + E_{so}\delta E_{bi} + \frac{9}{4}(\delta E_{bi})^2}$$

(V-18.c) $$E_{splitoff} = -\frac{E_{so}}{6} + \frac{\delta E_{001}}{4} - \frac{1}{2}\sqrt{E_{so}^{\ 2} + E_{so}\delta E_{001} + \frac{9}{4}(\delta E_{001})^2}$$

The heavy hole band becomes the highest VB. Analogously, the Hering Vogt Hamiltonian (V-12) simplifies to:

(V-19.a)

$$\Delta E_c^{001} = \Xi_2 \begin{pmatrix} 0 \\ 0 \\ 1 \end{pmatrix} * \left\{ \begin{pmatrix} \varepsilon_{xx} & 0 & 0 \\ 0 & \varepsilon_{xx} & 0 \\ 0 & 0 & \varepsilon_{zz} \end{pmatrix} - \frac{1}{3}(\varepsilon_{xx} + \varepsilon_{xx} + \varepsilon_{zz})\vec{1} \right\} * \begin{pmatrix} 0 \\ 0 \\ 1 \end{pmatrix} = \Xi_2 \frac{2}{3}(\varepsilon_{zz} - \varepsilon_{xx})$$

for the two <001> valleys and

(V-19.b) $$\Delta E_c^{010} = \Delta E_c^{100} = -\Xi_2 \frac{1}{3}(\varepsilon_{zz} - \varepsilon_{xx})$$

for the<100> and <010> valleys. All the shear strain components are zero, i.e. there is no coupling between Δ_1 and $\Delta_{2'}$. The lowest CB lies along the <001> valleys. The hydrostatic energy shift is readily obtained from equation (V-9). The utilized deformation potential constants are given in the table below.

Deformation potential			**Si**	**$Si_{0.7}Ge_{0.3}$**
VB:	b*	: tetragonal	b = -1.36 eV [63H]	b = -1.61 eV [74H]
	d*	: rhombohedral	d = -3.09 eV [63H]	d = -3.49 eV [74H]
	E_{SO}	: spin- orbit	E_{SO} = 0.044 eV [63H]	E_{SO} = 0.115 eV [63H]
CB:	Ξ_2	: linear splitting	Ξ_2 = 9.2 eV [66B]	Ξ_2 = 9.2 eV [66B]
	Ξ^*_2	: Δ_1, Δ_2 coupling	Ξ^*_2 = 9.5 eV [65H]	Ξ^*_2 = 9.5 eV [65H]
	Ξ_1	: hydrostatic	Ξ_1 = 3.8 eV [66B]	Ξ_1 = 3.8 eV [66B]

Table V-3: *Deformation potential constants for Si and* $Si_{0.7}Ge_{0.3}$

The results of the preceeding calculations are plotted in Fig. V-3. (a) for Si and (b) for SiGe. The lines show the splitting of the three valence bands (solid lines), the hydrostatic energy shift (dashed line) and the conduction band splitting (dotted lines) under external biaxial (001) tension. The vertical axis is broken between the scale for the valence and the conduction bands since no predictions about the absolute energy difference between these two bands is made. In the case of Si, the light hole and the splitoff band couple and shift together to lower energy (eqn V-18) while the heavy hole moves to higher energy. In case of a type I/II transition, the superscripts I/II mark the relevant CBs and VBs. The

* The valence band deformation potentials are often given by:

$$D_u = -\frac{3}{2}b\,;\;\; D_u' = -\frac{1}{2}\sqrt{3}d$$

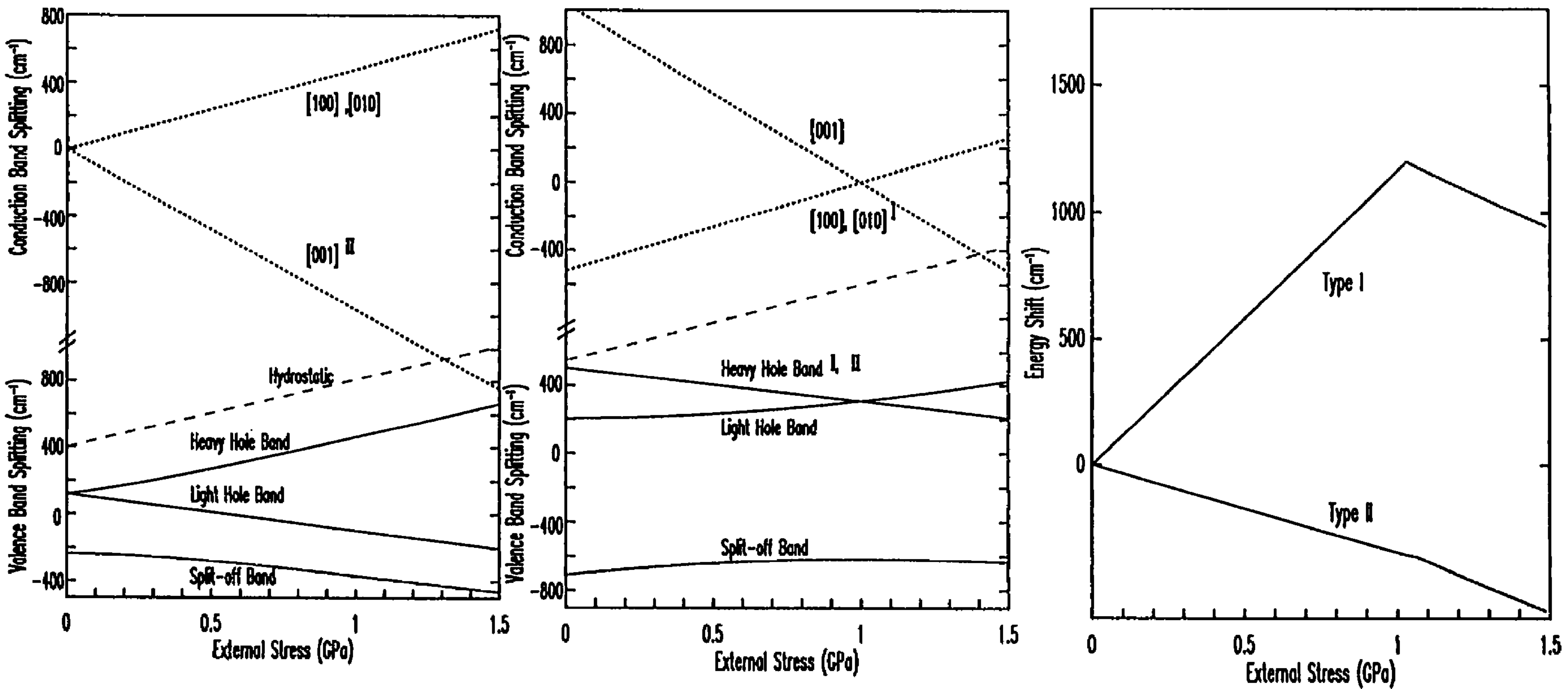

Figure V-3: *Theoretical Behavior of the Si and SiGe energy bands under biaxial strain*

Theoretical splitting of the VBs (solid lines) and CBs (dotted lines) and relative shifting of the centers of mass of the bands in (a) Si and (b) $Si_{0.7}Ge_{0.3}$ for external biaxial (001) tension. The SiGe PL moves in opposite directions for type I and type II band alignments.

effects of the built-in biaxial compression in the SiGe is reversed by the external biaxial tension. The important implication for our experiments is evident in Fig. V-3(c). For different band alignments, the SiGe PL moves in *opposite* directions. *This establishes a direct experimental test for the band alignment of the Si/SiGe interface.* Notice, that the Δ_C becomes more type II-like under increasing biaxial tension, since the lowest CBs in the Si and the alloy move in opposite directions.

V.C.2.Uniaxial Strain :

Uniaxial external stress is treated analogously to biaxial stress. The mathematical procedures are more involved for this strain configuration, since pulling along the [110] direction reduces the crystal symmetry of the Si and SiGe to base-centered orthorhombic (Fig. V-2 c,d). All three valence bands couple in this geometry. The Kleiner-Roth Hamiltonian becomes:

(V-20) $$H_{K-R} = -\frac{3}{4}\delta E_{001}\left(L_z^2 - \frac{L^2}{3}\right) - \sqrt{3}d\frac{S_{44}}{4}T[L_xL_y + L_yL_x]$$

The angular momentum L is rotated so that the [110] direction becomes the z-axis. The rotation matrix is [68P]:

(V-21) $$\tilde{\bar{L}} = \begin{pmatrix} 0 & 0 & 1 \\ 2^{-\frac{1}{2}} & -2^{-\frac{1}{2}} & 0 \\ 2^{-\frac{1}{2}} & 2^{-\frac{1}{2}} & 0 \end{pmatrix}\bar{L}$$

The Kleiner-Roth Hamiltonian (V-20) becomes:

(V-22) $$H_{K-R} = \frac{1}{4}\delta E_{001}\left(3\mathcal{I}_x^2 - \mathcal{I}^2\right) - \sqrt{3}d\frac{S_{44}}{4}T[\mathcal{I}_z^2 - \mathcal{I}_y^2]$$

With the matrix [71L]:

(V-23)
$$\begin{array}{cccc} & |3/2,3/2\rangle & |3/2,-1/2\rangle & |1/2,-1/2\rangle \end{array}$$
$$H = H_{spin-orbit} + H_{KR} = \begin{pmatrix} \frac{E_{so}}{3} - \frac{\delta E_{110}}{2} & -\frac{1}{8}\sqrt{3}\delta E & \frac{1}{8}\sqrt{6}\delta E \\ -\frac{1}{8}\sqrt{3}\delta E & \frac{E_{so}}{3} + \frac{\delta E_{110}}{2} & \frac{\sqrt{2}}{2}\delta E_{110} \\ \frac{1}{8}\sqrt{6}\delta E & \frac{\sqrt{2}}{2}\delta E_{110} & -\frac{2E_{so}}{3} \end{pmatrix}$$

where: $\delta E_{110} = \frac{1}{4}\left(2\delta E_{001} + 6\sqrt{3}d\varepsilon_{xy}\right)$ and $\delta E = \left(\delta E_{001} - 2\sqrt{3}d\varepsilon_{xy}\right)$.

The matrix is considerably more complicated than in the biaxial case. It is important to note, that $\pm m_J$ is no longer a good quantum number, i.e. [110] stress couples the heavy hole to the light hole and splitoff bands of opposite m_J sign. The matrix can be simplified by comparing the relative sizes of δE_{110} and δE. Substituting the strain components from Table V-2 and the deformation potential values from Table V-3 in δE_{110} and δE yields:

	δE_{110} $\left[\frac{10^{-12} cm^2\, eV}{dyn}\right]$	δE $\left[\frac{10^{-12} cm^2\, eV}{dyn}\right]$	$\frac{\delta E}{\delta E_{110}}$
Si	2.43*T	0.14*T	6%
$Si_{0.7}Ge_{0.3}$	2.09*T	0.12*T	6%

Table V-4: *Numerical comparison between δE110 and δE*

Obviously, the coupling of the heavy hole band with the other VBs can be treated as a perturbation. The lower right (2x2) matrix of the unperturbed Hamiltonian is

diagonalized and the weak coupling with the heavy hole is afterwards added using second order perturbation theory. The solutions for the eigenvalues up to second order were taken directly from Laude *et al.* [71L] and are plotted in Fig. V-4 . The explicit formulae are not given here, since their analytical form is long and all relevant physics is visible in the plot. The linear splitting of the CB is given by equations V-19 (a) and (b), by substituting the appropriate strain components from Table V-2. As $\varepsilon_{xy} \neq 0$, stress along [110] induces a quadratic energy shift due to the coupling between the Δ_1 and Δ_2 bands. Eqn V-14 applies. The hydrostatic shift is readily obtained from eqn V-9 and Table V-2.

The uniaxial case shown in Fig. V-4 is completely analogous to the biaxial case shown in Fig. V-3. Due to the coupling of all three subbands, the magnitude of the VB splitting is smaller than in the biaxial case. Again, the shifts have opposite signs for type I and type II band alignments.

V.D.Summary:

Deformation potential theory predicts distinct behaviors for SiGe PL from a strained sample depending on whether type I or type II band alignments exist. External tensile strain induced by our bending rigs is expected to shift the SiGe PL signal in opposite directions for the two cases.

The slopes of the energy shifts versus strain, shown in Fig. V-3(c) and V-4(c), quantify the magnitude of the shifts.

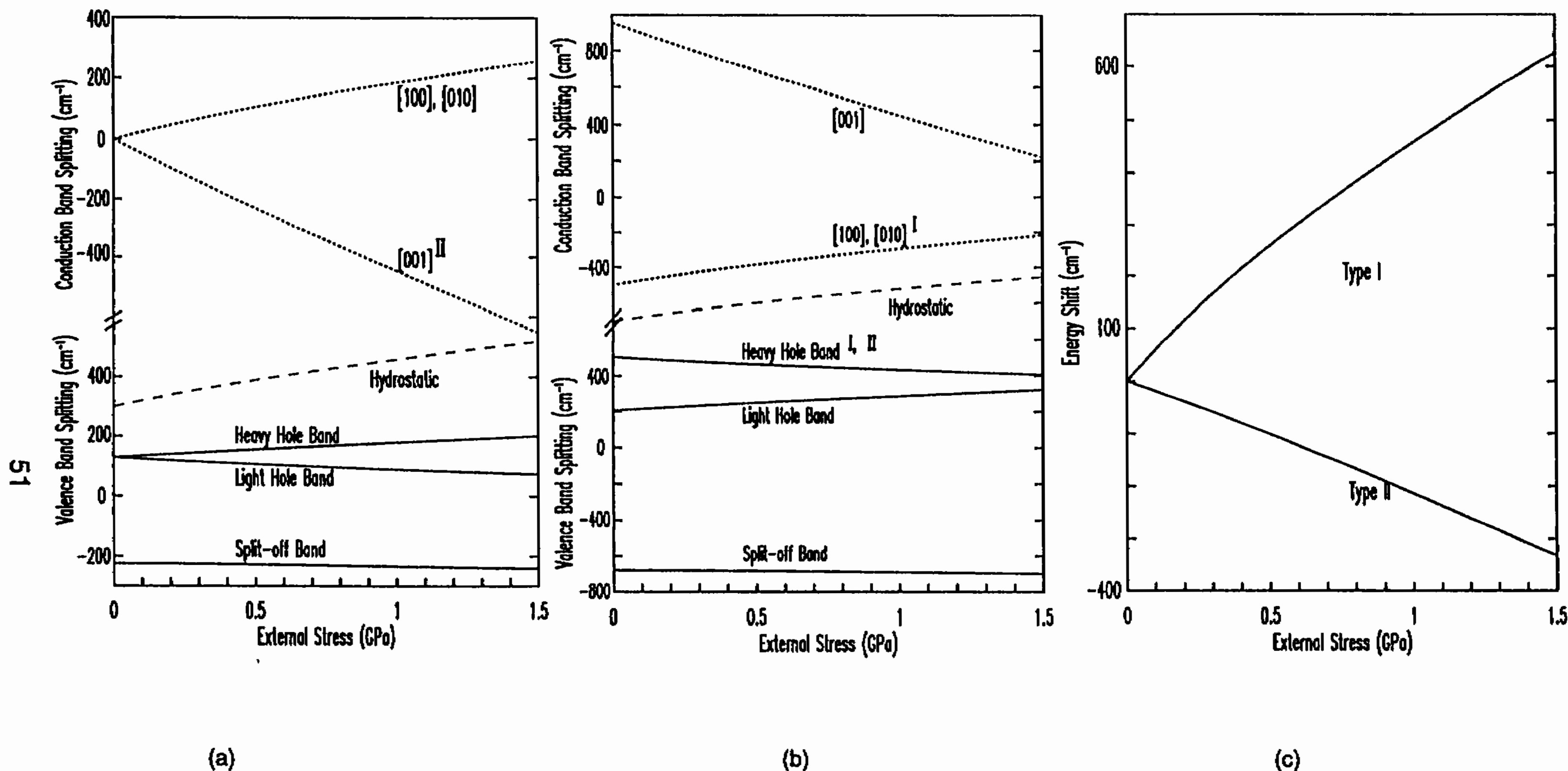

Figure V-4: *Theoretical Behavior of the Si and SiGe energy bands under uniaxial strain*

Theoretical splitting of the VBs (solid lines) and CBs (dotted lines) and relative shifting of the centers of mass of the bands in (a) Si and (b) $Si_{0.7}Ge_{0.3}$ *for external uniaxial [110] tension. The SiGe PL moves in opposite direction for type I and type II band alignments.*

VI. Experimental Results and Discussion

In the preceeding sections we have developed the theoretical framework to properly interpret our experimental results. Sections VI-A through VI-D present various experimental results that suggest a type II band alignment in the investigated Si/SiGe QW.

VI.A. Energy Shifts of the SiGe PL under external strain

Are the electrons that generate the SiGe PL located in the Si or in the SiGe? For a type I band alignment, the SiGe NP line should blueshift with increasing [110] or (001) tensile stress. A redshift would indicate a type II alignment. Our experimental results are presented in Fig. VI-1. Shown are the energy shifts of the SiGe NP line for different excitation densities versus applied tensile strain. All energies are relative to that of the NP line under zero external stress and illumination with 10^{-7} I_o (I_o = 10 Wcm^{-2}). The solid and dashed lines show the theoretical shifts calculated in section V for type I and type II transitions, respectively. Only the slopes of the lines are relevant. The qualitative behavior is the same for both bending arrangements. The uniaxial bending results have been included to allow a direct comparison with the data of Houghton *et al.* [95H] who performed the same experiment under a constant excitation density around ~ 100 $mWcm^{-2}$. At that intensity, our sample also

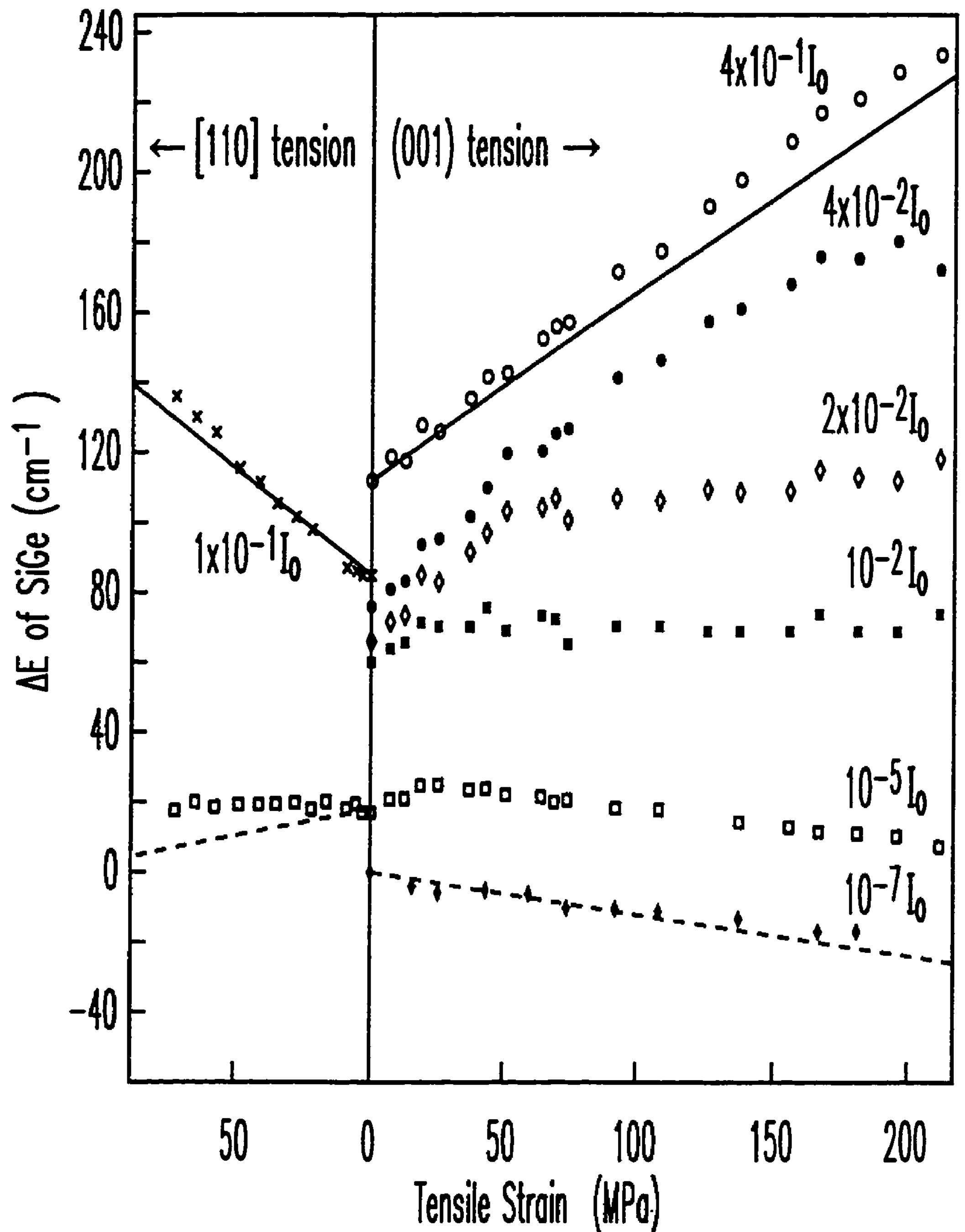

***Figure VI-1:** Experimental and Theoretical Energy Shifts of SiGe under external strain*

The energy shift of the SiGe NP line over a wide range of excitation densities plotted versus applied tensile strain. All energies are relative to the NP line under zero external strain and illumination with $10^{-7} I_0$ ($I_0 = 10$ Wcm^{-2}). Solid (dotted) lines are theoretical predictions for the strain dependence of the energy shifts of type I (type II) transitions for a $Si_{0.7}Ge_{0.3}$ /Si(001) QW, as calculated in section V.

exhibited type I band behavior in agreement with the results obtained by Houghton *et al.* Fig. VI-1 reveals that the physics of the interface is strongly dependent on the illumination density. Although our sample exhibited type I characteristics under high illumination conditions, this behavior became type II in nature as the excitation power density was reduced! To understand this behavior, *band bending* must be considered. Fig. VI-2 schematically shows the effect of varying excitation densities on the band structure of the interface. In Fig. VI-2(a) we assume an initial type II band alignment under a low illumination density. The solid lines denote the lowest CBs and highest VBs. The dashed lines represent the probability functions for the holes and electrons. The electrons and holes localize in the Si and SiGe, respectively. In Fig. VI-2(b), the excitation density is increased and charge accumulation in the SiGe and Si leads to band bending of the CBs and VBs. Δ_V is much larger than Δ_C, i.e. the holes are more efficiently confined than the electrons and produce stronger band bending. In the presence of a sufficiently large charge carrier density, the band bending outweighs the original CB offset and the interface effectively becomes type I, or in other words, the charge of the holes draws the electrons into the QW, overcoming the CB offset. This simple model explains Houghton's type I experimental results, which were collected under elevated excitation powers, and provides the key element to understanding Fig. VI-1. The unperturbed sample exhibits type II behavior at low excitation densities ($10^{-7}I_0$). As the excitation density is increased, band bending renders the PL type I and the NP line

blueshifts under small tensile strains. For a given excitation level, above a *"changeover-strain"* the PL again becomes type II. Recall from section V, that tensile strain increases the magnitude of a type II Δ_C. The changeover-strain therefore increases with increasing excitation powers, i.e. a larger Δ_C is necessary to outweigh the band bending. For the highest excitations in Fig. VI-1 we did not reach the changeover strain since the sample broke at a stress of 220 MPa.

VI.B.Time-resolved PL

The foregoing discussion has demonstrated type II band alignment from the observed shifts of the SiGe NP lines. The time dependence of the SiGe PL signal supports this conclusion. Fig. VI-3 presents the decay of the SiGe PL signal versus time under conditions of zero external stress. At low excitation densities, long-lived excitons with lifetimes in the ms range exist. With growing illumination intensities the excitons are joined by a much shorter-lived signal component (several μs). This contribution to the total PL signal finally dominates over the long-lived excitons by as much as two orders of magnitude. We attribute the short-lived signal to the recombination of excitons. Its appearance at these power densities is in accord with the previous results. For a type II band alignment in an indirect semiconductor heterostructure, the recombining holes and electrons are separated both in real space and in momentum space. This causes extremely long lifetimes. As the interface becomes type I, the electron

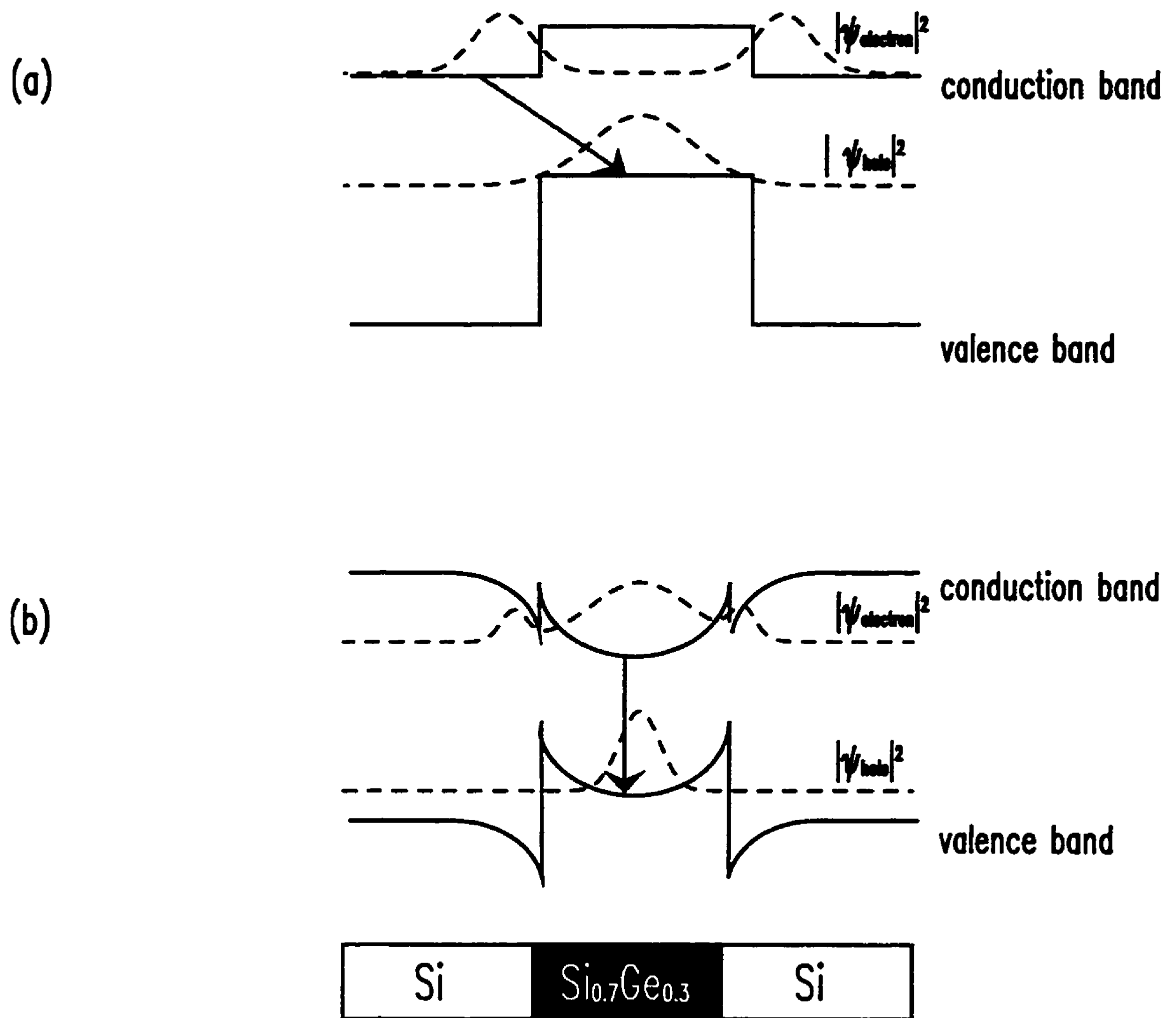

Figure VI-2: *Qualitative Model of Band Bending*

Band bending due to charge accumulation under high excitation densities. Under low excitation densities (a), the interface is type II. The effective confinement of holes in the SiGe bends the CB and VB down, finally rendering the interface type I.

wave-functions move into the alloy layer (Fig. VI-2). The resulting short-lived excitons have been reported before [93L].

Under applied stress, the decay times exhibited the same behavior as in the absence of strain, but the longer-lived PL components were observed at higher excitation levels at high strain, as expected.

VI.C.Type I/Type II spectra

Further evidence for our model can be found by analyzing the features in the PL spectra as it changes form type I to type II.

In Fig. VI-4, the SiGe PL spectra under 180 MPa biaxial tension are plotted versus excitation power over eight orders of magnitude ($I_0 = 10 \text{ Wcm}^{-2}$). All the features in the I_0 and $10^{-1} I_0$ spectra have been previously reported and were discussed in section III-C. The NP line is the most prominent feature due to alloy scattering. A weak TA replica is resolved, accompanied by the three TO replicas due to the Si-Si, Si-Ge and Ge-Ge bonds. The relative intensities of the TO replicas reflect the relative number of respective nearest neighbors in the alloy. Changing from I_0 to $10^{-1} I_0$ slightly redshifts the entire spectrum. This small effect may be attributed to band filling (i.e. if the lowest states in the CB and VB become filled under high excitation powers, the transition energies increase) .

The type I/II transition occurs between $10^{-1} I_0$ and $10^{-2} I_0$ and is accompanied by a drastic change in the PL spectrum. Further reduction in the excitation density does not alter the spectrum significantly. We denote the spectra from $10^{-2} I_0$ to $10^{-7} I_0$ as *"type II spectra"*. The downshift of the transition

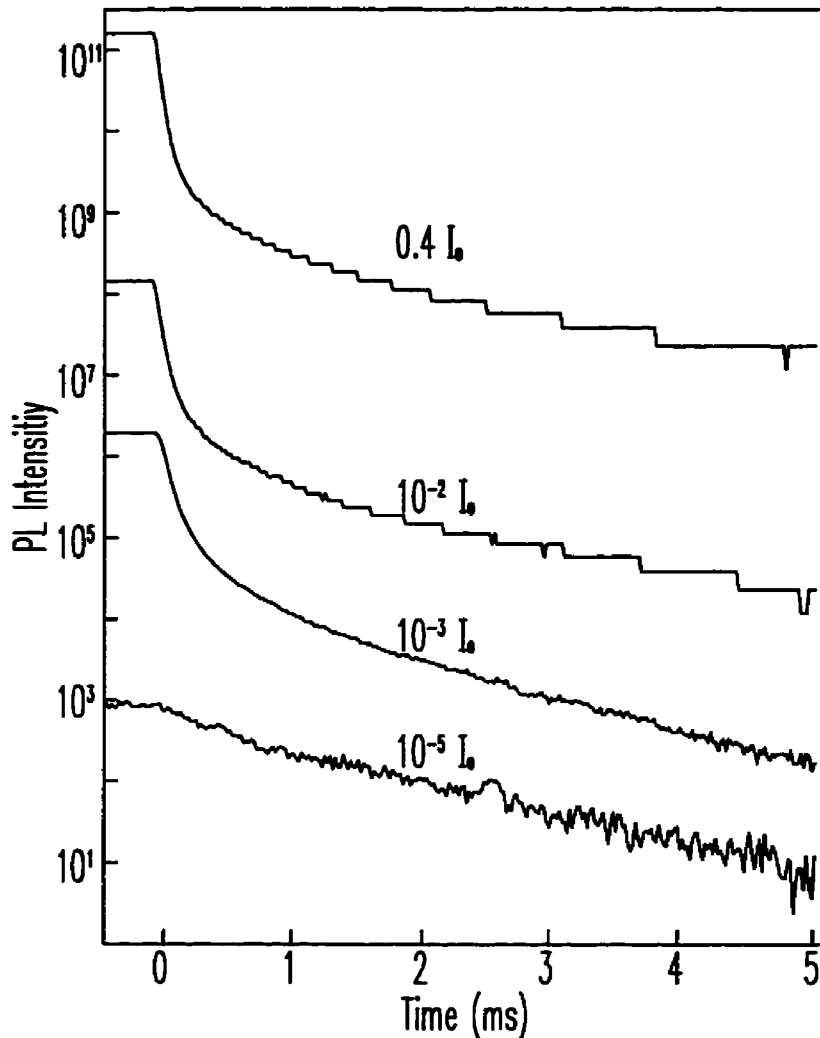

Figure VI-3: *Decay of the SiGe PL signal with time*

Decay of the SiGe PL signal with time for various excitation densities while under zero external strain.

between 10^{-1} I_0 and 10^{-2} I_0 is very abrupt since the magnitude of charge accumulation is proportional to both the carrier lifetimes and the excitation density. The former change from ms to μs in the region of the type II to type I transition, so that the charge density in the alloy almost saturates above the transition. The redshift indicates that the electrons move from the SiGe QW into

the Si barriers, yielding a decreased transition energy as schematically shown in Fig. VI-2. The magnitude of the downshift corresponds in first order to Δ_C.

(VI-1) $$\Delta_C = 23 \pm 8 meV$$

This thesis presents the first report of type II PL from a SiGe/Si QW. The type II spectrum exhibits features which are distinctly different from those associated with the ubiquitous type I spectrum. Most striking is the dramatic enhancement of the intensity of the TA replica relative to the Si-Si TO replica. Although we have not found a satisfying explanation for this increase, we will show that it is a clear "finger-print" of the type II regime. The possibility, that the TA replica is superimposed on a LE can be excluded, since no TO replica is present at the relevant energy below the TA. The change in the TO region of the spectrum is easier to interpret. In type II spectra the Si-Ge and Ge-Ge TO replicas disappear, leaving just the Si-Si TO mode. This is due to the electron wave function being primarily in the Si. Hence, the number of radiative recombinations involving Si-Ge and Ge-Ge modes is reduced.

Figure VI-5 allows for a more detailed comparison of the type I and type II spectra. The three spectra have been recorded under zero external strain. The solid and dashed lines show the 30 Å $Si_{0.7}Ge_{0.3}$ QW under high and low illumination conditions. The dotted line is the type I spectra from a thick, 360 Å $Si_{0.75}Ge_{0.25}$ QW under high illumination power, grown by conventional CVD. The NP peaks are aligned to facilitate comparison of the spectra. Just as in the low

power, strained PL spectra of Fig. VI-4, the type II spectrum in Fig. VI-5 exhibits a large TA peak and suppressed Si-Ge, Ge-Ge TO modes. The thick QW has a 123 cm^{-1} TA replica which is characteristic for $Si_{0.75}Ge_{0.25}$ [89Wb] while the TA replica in the type II spectrum lies at the 153 cm^{-1} TA energy of pure Si. The TA region in the type I spectra of the thin QW is a mixture composed of both Si and SiGe TA modes. This indicates spreading of the electron wave-function into the Si barrier which is suppressed for wide QWs. Hence, everything is consistent with our model.

VI.D.The TA/TO_{Si-Si} ratio in type I/II spectra

Recall that the TA intensity is enhanced in type II spectra relative to the intensity of the Si-Si TO replica. The inset of Fig. VI-5 confirms the results of Fig. VI-1 and shows that a large TA/TO_{Si-Si} ratio is in fact an identifiable signature of type II band alignment. The inset displays the TA/TO ratio over a wide range of excitation densities for three different strains: (a) zero, (b) moderate strain (90 MPa) and (c) high (170 MPa) strain. For all strains, the ratio has to the same limits; 0.4 for type I and 0.8 for type II. As the strain is increased, the changeover between the two regimes takes place at increasing excitation densities which agrees with the results of section VI-A.

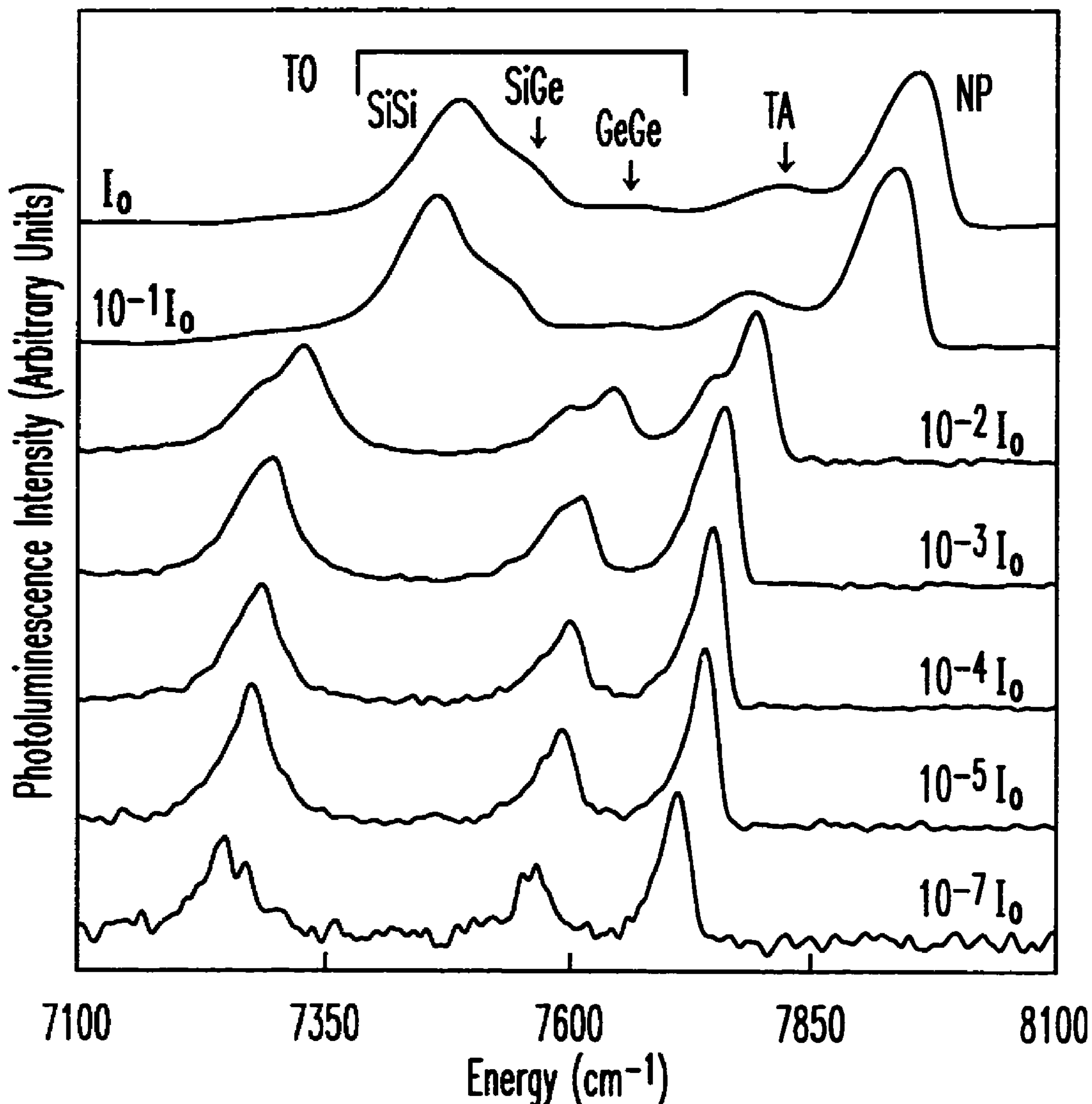

Figure VI-4: *PL spectra versus excitation density from strained SiGe/Si*

PL spectra at 1.6 K from a $Si_{0.7}Ge_{0.3}$/Si QW under a biaxial tension of 180 MPa. The NP, TA and 3 TO phonon replicas transitions are labeled in the high excitation spectrum (I_0 = 10 Wcm^{-2}). At this stress the changeover occurs near 10^{-2} I_0.

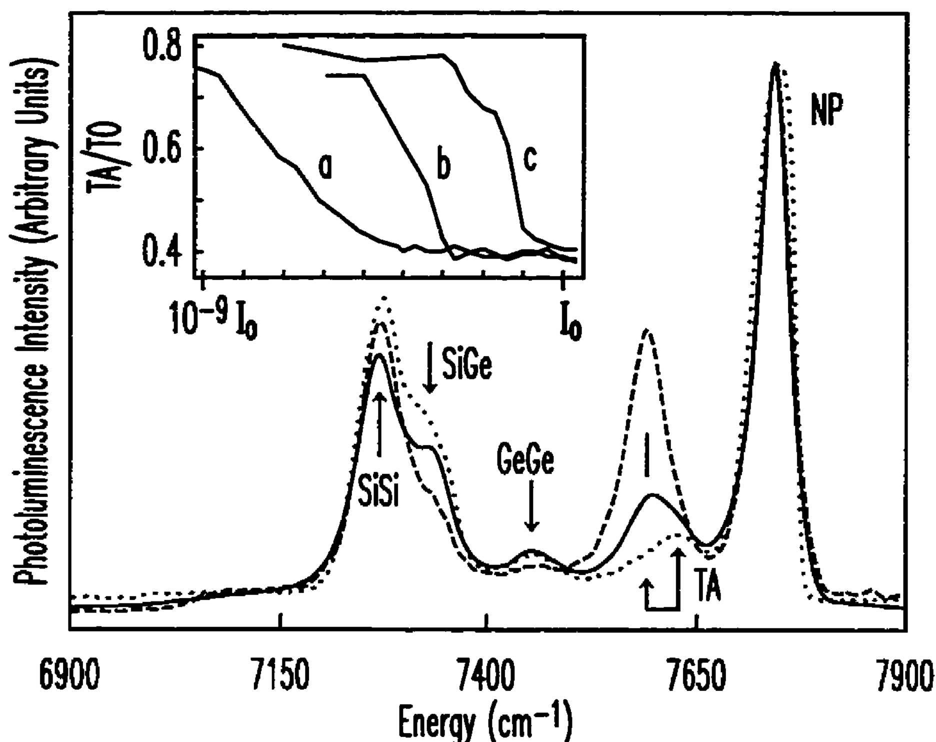

Figure VI-5: *Type I/II spectra from various SiGe QW samples*

PL from the $Si_{0.7}Ge_{0.3}$/Si QW sample at two different excitation densities in the absence of external strain. The solid curve corresponds to an excitation densities of 10^{-2} I_0 while the dashed curve corresponds to $5x10^{-8}$ I_0. The dotted curve displays the PL from a thick (360 Å) $Si_{0.75}Ge_{0.25}$/Si QW grown by conventional CVD. The type I spectra have been slightly downshifted to align the three NP peaks.
The inset shows the intensity ratio of the TA peak relative to the Si-Si TO peak over a wide range of excitation densities. Curves a, b, c, correspond to zero, moderate (90 MPa) and high (170 MPa) external biaxial (001) strain, respectively.

VI.E. Discussion

Sections VI-A to VI-D confirm type II band alignment in a pseudomorphically grown $Si_{0.7}Ge_{0.3}$ on Si(001) single QW sample under low excitation conditions. Our results resolve the question as to the type of band

alignment in any strained SiGe/(001)Si QW system. The investigated heterostructure is an important prototype, since future SiGe-based devices will preferably have Si substrates, so that they can be directly integrated using conventional Si processing technology.

We have shown that band bending can change the band alignment from type II to type I at moderate excitation powers. This explains, why type II spectra have not been reported before. Our experimental setup allowed for PL spectroscopy at extremely low excitation powers from a high quality sample. The Ge-Array-based dispersive spectrometer enabled us to collect PL spectra under excitation densities below the μWcm^{-2} level and the Si/SiGe interface of the sample was practically dislocation-free as could be inferred from the absence of broad subbands in the PL spectra.

For future device applications it will be important to carefully consider the impurity concentration throughout the heterostructure, since high acceptor densities in Si generate positive charge accumulation in the SiGe potential well and induce band bending. This could result in a type I band alignment in Si/SiGe systems in the absence of any external excitation.

VI.F. Summary and Outlook

Under low excitation densities the PL line shift of the SiGe NP transition showed clear type II behavior in a high purity, dislocation-free sample. This evidence was supported by long-lived type II excitons and prominent spectral changes at the type I/II transition. All of these different aspects indicate that the band alignment of pseudomorphically grown SiGe/(001)Si is in fact type II. The nature of this interface may play an important role when designing future devices. A remaining physical question concerns the origin of the enhanced TA replica in the type II spectrum.

Finally, while an important physical question has been resolved, further experimental and theoretical studies are necessary to complete our understanding of Si/SiGe heterostructures.

References:

[97T] M. L. W. Thewalt, D. A. Harrison, C. F. Reinhart, J. A. Wolk, H. Lafontaine, "Type II Band Alignment in $Si_{1-x}Ge_x/Si(001)$ Quantum Wells: The Ubiquitous Type I Luminescence Results from Band Bending", submitted to Phys. Rev. Lett.

[96A] A. A. St. Amour, "Growth and Photoluminescence of Crystalline $Si_{1-x}Ge_x/Si$ and $Si_{1-x-y}Ge_xC_y/Si$ Heterostructures", Ph.D. Thesis, Princeton University (1996)

[96L] H. Lafontaine, D. C. Houghton, D. Elliot, N. L. Rowell, J.-M. Baribeau, S. Laframboise, G. I. Sproule, S. J. Rolfe, J. Vac. Sci. Technol. **B 14** (3), 1675 (1996)

[96H] D. A. Harrison, V. A. Karasyuk, M. L. W. Thewalt, D. J. S. Beckett, and A. J. Spring Thorpe, in Proceedings of The 23rd International Conference on the Physics of Semiconductors, edited by M. Scheffler and R. Zimmermann, (World Scientific, Singapore, 1996), Vol. 1, p. 381.

[96M] R. A. Metzger, Compound Semiconductor, p.25 (Nov/Dec 1996)

[95H] D. C. Houghton, G. C. Aers, S.-R. Eris Yang, E. Wang, N. L. Rowell, Phys. Rev. Lett. **75** (5), 866 (1995)

[95S] A. Schueppen, H. Dietrich, J. Crystal Growth **157**, 207 (1995)

[95M] R. A. Metzger, Compound Semiconductor, p. 21 (Nov/Dec 1995)

[95U] N. Usami, Y. Shiraki, S. Fukatsu, J. of Crystal Growth **157**, 27 (1995)

[94B] T. Baier, U. Mantz, K. Thonke, R. Sauer, F. Schaeffer, H.-J. Herzog, Phys. Rev. **B 50**(20), 15191 (1994)

[94C] M. R. Caymax, W. Y. Leong in "Advanced Silicon & Semiconducting Silicon-Alloy Based Materials & Devices", The Institute of Physics, London, p.141 (1994)

[94S] R. Shankar, "Principles of Quantum Mechanics", Plenum Press, New York, (1994)

[94M] U. Mantz, K. Thonke, R. Sauer,F. Schaeffler, H.-J. Herzog, "Photoluminescence Studies of Pseudomorphic $Si_{1-x}Ge_x$ Alloys under External Uniaxial Stress", ICPS 92, 1556 (1992)

[93F] S. Fukatsu, Y. Shiraki, Appl. Phys. Lett. **63**(17), 2378 (1993)

[93G] E. R. Glaser, T. A. Kennedy, D. J. Godbey, P. E. Thompson, K. L. Wang, C. H. Chern, Phys. Rev. **B 47**(3), 1305 (1993)

[93L] L. C. Lenchyshyn, M. L. W. Thewalt, D. C. Houghton , J.-P. Noel, N. R. Rowell, J. C. Sturm, X. Xiao, Phys. Rev. **B 47**(24), 16655 (1993)

[93R] M. M. Riegler, P. Vogl, Phys. Rev. **B 48**(19), 14276 (1993)

[92L] L. C. Lenchyshyn, M. L. W. Thewalt, J. C. Sturm, P. V. Schwartz, E. J. Prinz, N. L. Rowell, J.-P. Noel, D. C. Houghton, Appl. Phys. Lett. **60**(25), 3174 (1992)

[92N] G. A. Northrop, J. F. Morar, D. J. Wolford, J. A. Bradley, J. Vac. Sci. Technol. **B 10**(4), 2018 (1992)

[92S1] J. Spitzer, K. Thonke, R. Sauer, H. Kibbel , H.-J. Herzog, E. Kasper, Appl. Phys. Lett. **60**(14), 1729 (1992)

[92W] M. Wachter, K. Thonke, R. Sauer, F. Schaeffer, H.-J. Herzog, E. Kasper, Thin Solid Films **222**, 10 (1992)

[91C] L. Colombo, R. Resta, S. Baroni, Phys. Rev. **B 44**, 5572 (1991)

[91R] D. J. Robbins, L. T. Canham, S. J. Barnett, A. D. Pitt, P. Calcott, J. Appl. Phys. **71**(3), 1407 (1991)

[91R1]D. J. Robbins, J. L. Glasper, A. G. Cullis, W. Y. Leong, J. Appl. Phys. **69**(6), 3729 (1991)

[90S] J. C. Sturm,H. Manoharan, L. C. Lenchyshyn, M. L. W. Thewalt, N. L. Rowell, J.-P. Noël, D. C. Houghton, Phys. Rev. Lett. **66**(10), 1362 (1991)

[90P] G. L. Patton, J. H. Comfort, B. S. Meyerson, E. F. Crabbe, G. J. Scilla, E. de Fresart, J. M. C. Stork, J. Y.-C. Sun, D. L. Harame, J. N. Burghartz, IEEE Electron Device Letters, **11**(4), 171 (990)

[89Wb] J. Weber, M. I. Alonso, Phys. Rev. **B 40**(8), 5683 (1989)

[88vdW] C. G. van der Walle, Phys. Rev. **B 39**(3), 1871 (1988)

[86M] B. S. Meyerson, Appl. Phys. Lett. **48**(12), 797 (1986)

[86vdW] C. G. van der Walle, R. M. Martin, Phys. Rev. **B 34**(8), 5621 (1986)

[84A] G. Abstreiter, H. Brugger, T. Wolf, H. Jorke, H.-J. Herzog, Phys. Rev. Lett. **54**(22), 2441 (1985)

[84D] R. Dingle, IEEE Transaction on Electron Devices, Vol. ED-31 (11), 1662 (1984)

[85B] J. C. Bean, Science **230**(4722), 127 (1985)

[85L] D. V. Lang, R. People, J. C. Bean, A. M. Sergent, Appl. Phys. Lett. **47**(12), 1333 (1985)

[85P] R. People, Phys. Rev. **B 32**(2), 1405 (1985)

[85P1] R. People, Appl. Phys. Lett. **47**(3), 322 (1985)

[85P2] R. People, J. C. Bean, Appl. Phys. Lett. **48**(8), 538 (1985)

[84M] M. A. Green, "Silicon Solar Cells: Operating Principles, Technology and System Application", National Library of Australia (1995)

[84P] R. People, J. C. Bean, D. V. Lang, A.M. Sergent, H. L. Stroemer, K. W. Wecht, R. T. Lynch, K. Baldwin, Appl. Phys. Lett. **45**(11), 1231 (1984)

[81W] R. C. Weast (Editor), "CRC Handbook of Chemistry and Physics", 61st edition, CRC Press, Inc. (1981)

[76H] R. Hertzberg in "Deformation and Fracture Mechanics of Engineering Materials", 12 (1976)

[74H] J. C. Hensel, K. Suzuki, Phys. Rev. **B 9**, 4219, (1974)

[72B] W. A. Brantley, J. Appl. Phys., Vol. **44**(1), 534 (1972)

[71L] L. D. Laude, F.H. Pollack, M. Cardona, Phys. Rev. **B 3**, 2623 (1971)

[69C] J. F. Cornwell, "Group Theory and Electronic Energy Bands in Solids", John Wiley & Sons (1969)

[69S] S. M. Sze in " the Physics of Semiconductor Devices", John Wiley & Sons, Inc. (1969)

[68P] F. H. Pollack, M. Cardona, Phys. Rev. **172**(3), 816 (1968)

[67K] E. O. Kane in "Semiconductors and Semimetals", Academic New York, Vol.1, 75 (1967)

[66B] I. Balsev, Phys. Rev. **143**(2), 636 (1965)

[65H] J. C. Hensel, H. Hasegawa, N. Nakayama, Phys. Rev. **138**, A225 (1965)

[63H] J. C. Hensel, G. Fehler, Phys. Rev. **129**, 1041 (1963)

[59K] W. H. Kleiner, L. M. Roth, Phys. Rev. Let. **2**(2), 334 (1959)

[56H] C. Herring, E. Vogt, Phys. Rev. **101**, 944 (1956)

[54K] C. Kittel, "Introduction to Solid State Physics", John Wiley & Sons (1954)

[1892L] A. E. H. Love in "The Mathematical Theory of Elasticity", New York Dover Publications, 160 (1944)

[BM] Bomem Inc., Hartmann & Braun, 450 St.- Jean Baptiste, Québec, Québec G2E 5S5

TEST TARGET (QA-3)

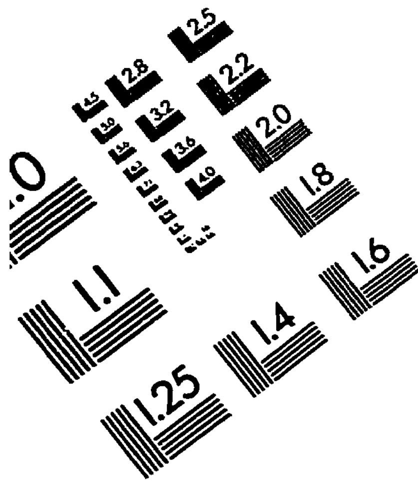

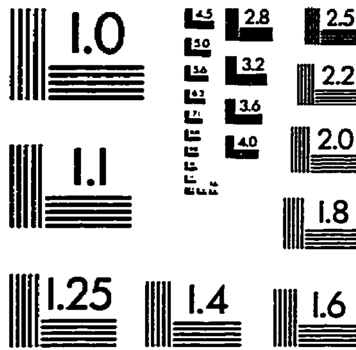
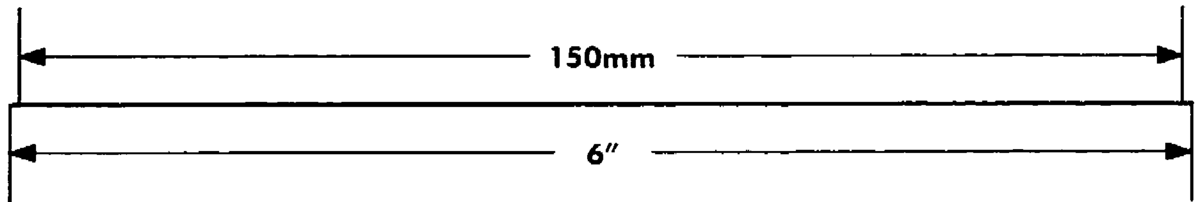

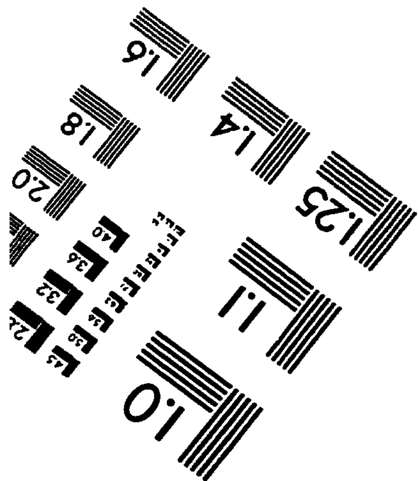

APPLIED IMAGE, Inc
1653 East Main Street
Rochester, NY 14609 USA
Phone: 716/482-0300
Fax: 716/288-5989

© 1993, Applied Image, Inc., All Rights Reserved